

A New Open-Source Code for Spherically-Symmetric Stellar Collapse to Neutron Stars and Black Holes

Evan O'Connor

E-mail: evanoc@tapir.caltech.edu
TAPIR, Mail Code 350-17,
California Institute of Technology, Pasadena, California 91125, USA

Christian D Ott

E-mail: cott@tapir.caltech.edu
TAPIR, Mail Code 350-17,
California Institute of Technology, Pasadena, California 91125, USA
and
Niels Bohr International Academy, The Niels Bohr Institute,
Copenhagen, Denmark
and
Center for Computation and Technology, Louisiana State University,
Baton Rouge, LA, USA

Abstract. We present the new open-source spherically-symmetric general-relativistic (GR) hydrodynamics code **GR1D**. It is based on the Eulerian formulation of GR hydrodynamics (GRHD) put forth by Romero-Ibañez-Gourgoulhon and employs radial-gauge, polar-slicing coordinates in which the 3+1 equations simplify substantially. We discretize the GRHD equations with a finite-volume scheme, employing piecewise-parabolic reconstruction and an approximate Riemann solver. **GR1D** is intended for the simulation of stellar collapse to neutron stars and black holes and will also serve as a testbed for modeling technology to be incorporated in multi-D GR codes. Its GRHD part is coupled to various finite-temperature microphysical equations of state in tabulated form that we make available with **GR1D**. An approximate deleptonization scheme for the collapse phase and a neutrino-leakage/heating scheme for the postbounce epoch are included and described. We also derive the equations for effective rotation in 1D and implement them in **GR1D**. We present an array of standard test calculations and also show how simple analytic equations of state in combination with presupernova models from stellar evolutionary calculations can be used to study qualitative aspects of black hole formation in failing *rotating* core-collapse supernovae. In addition, we present a simulation with microphysical EOS and neutrino leakage/heating of a failing core-collapse supernova and black hole formation in a presupernova model of a $40\text{-}M_{\odot}$ zero-age main-sequence star. We find good agreement on the time of black hole formation (within 20%) and last stable protoneutron star mass (within 10%) with predictions from simulations with full Boltzmann neutrino radiation hydrodynamics.

PACS numbers: 04.25.D-, 04.40.Dg, 97.10.Kc, 97.60.Bw, 97.60.Jd, 97.60.Lf, 26.60.Kp

1. Introduction

Stellar core collapse is among the most energetic phenomena in the modern universe and liberates of the order of a few hundred [B]ethe ($1 \text{ B} = 10^{51} \text{ erg}$) of gravitational energy as the core of a massive star (zero-age main-sequence [ZAMS] mass $8-10 M_{\odot} \lesssim M \lesssim 100 M_{\odot}$) is compressed from a radius of $\sim 1500 \text{ km}$ and central density $\rho_c \sim 10^{10} \text{ g cm}^{-3}$ to $\sim 15 \text{ km}$ and ρ_c in excess of nuclear density. Most ($\sim 99\%$) of this energy is ultimately radiated in neutrinos, but a small fraction ($\sim 1 \text{ B}$) may be converted into kinetic and internal energy of an outgoing shock wave and may result in a core-collapse supernova explosion within the first seconds after collapse. The precise mode of conversion, the *core-collapse supernova mechanism*, is uncertain and has been the enigma of supernova theory for the past five decades (e.g., [1–8]). At the densities and velocities encountered in stellar collapse, the inclusion of general relativistic effects is not an optional model sophistication, but a necessity for quantitatively and qualitatively reliable results. Importantly, general relativity (GR) predicts that the protoneutron star (PNS) formed in the initial collapse will undergo a second gravitational instability and collapse to a black hole (BH), if continued accretion pushes it over the maximum mass supported by the strong force and nucleon degeneracy. This may happen if the supernova mechanism fails and no explosion is launched or due to fallback accretion if an explosion occurs, but is too weak to unbind the entire stellar envelope [9]. In both cases, and provided sufficient angular momentum and its appropriate distribution in the progenitor star, the newly formed *collapsar* may become the central engine for a long-soft gamma-ray burst (GRB) [10, 11].

General relativistic computational models of stellar collapse have a long pedigree, starting with the spherically-symmetric (1D) Lagrangian work of May & White in the mid-1960s [12], based on the comoving GR hydrodynamics formulation in orthogonal coordinates by Misner & Sharp [13] and using a finite-difference scheme with an artificial viscosity [14] approach to handle shocks. Much subsequent 1D GR work [15–20] was based on this or similar approaches, including full radiation-hydrodynamics stellar collapse and core-collapse supernova simulations with finite-temperature microphysical equations of state (EOS) [21–25]. Eulerian formulations, more suited for extension to multi-D simulations, were introduced later and used maximal slicing [26–29], or radial-gauge, polar-slicing (RGPS) [30]. These schemes, with the exception of [30], who employed pseudospectral methods, still used artificial viscosity approaches to shock treatment. More accurate, high-resolution shock-capturing (HRSC) approaches to GR stellar collapse based on higher-order Guderony schemes and Riemann solvers were introduced by Marti et al. [31] and Yamada [32] in the Lagrangian context, by Marti et al. [33] in the fixed-background Eulerian case, and by Romero et al. [34] and Noble [35] in the RGPS Eulerian frame. Yamada’s approach was later extended to include microphysical EOS and radiation transport [36, 37].ourgoulhon & Haensel [38] included an approximate neutrino transport treatment in their code. Preliminary results of Romero’s code with a microphysical EOS and a neutrino leakage scheme were published in [39, 40].

State-of-the-art simulations of stellar collapse and of the postbounce supernova evolution strongly suggest that multi-D dynamics is crucial for the core-collapse supernova mechanism to succeed in massive stars (e.g., [2, 4, 41–44]). Present multi-D core-collapse supernova codes are either Newtonian [44–46] or employ Newtonian

dynamics with relativistic corrections to the gravitational potential [3, 4, 7]. Multi-D simulations in conformally-flat [47] or full GR traditionally relied on simple analytic EOS and polytropic initial models and neglected crucial neutrino effects (see, e.g., [48–51]). Only recently have the first axisymmetric (2D) [52, 53] and 3D [54, 55] GR core collapse simulations become available that employ microphysical EOS and an approximate treatment of deleptonization in the collapse phase, but postbounce neutrino transport, cooling, and heating are still not taken into account in these models. However, very recently, Müller [56] has succeeded in implementing the complex and computationally-intensive radiation-transport scheme of [57] in the 2D conformally-flat GR framework of [48, 49] and first results are forthcoming [58].

In this article, we lay the foundations for a new and open approach to the stellar collapse and core-collapse supernova problem in GR. We discuss the formulation and implementation of the code **GR1D**, a new, spherically-symmetric Eulerian GR code for stellar collapse to neutron stars and black holes with approximate pre- and postbounce neutrino treatment. We release **GR1D** and all its microphysics and input physics as open source to be downloaded from <http://www.stellarcollapse.org>. It is meant to complement open-source 3D GR codes such as **Whisky** [59] that do not come with microphysics and neutrino approximations. At the same time, we intend **GR1D** to serve as an efficient 1D GR testbed for new modeling technology to be eventually incorporated in multi-D codes. In addition, **GR1D** and its microphysics components can readily be adapted for use in the computational modeling of problems involving some or much of the same physics as in the stellar collapse problem, e.g., the postmerger phase of double neutron-star or black-hole – neutron-star coalescence.

We base **GR1D** on the conceptually simple and computationally efficient RGPS formalism of [30]. **GR1D**, like the code of [34], employs a Eulerian formulation of GR hydrodynamics with HRSC and works on non-equidistant grids. For the first time in the 1D GR context, we derive and implement in **GR1D** an extension of the 1D GR hydrodynamics equations to include rotation in an effective fashion. For completeness and comparison of Newtonian and GR dynamics, **GR1D** also implements 1D Newtonian hydrodynamics. **GR1D** operates with analytic EOS as well as with tabulated microphysical EOS through a general EOS interface. We discuss and provide EOS tables for the EOS of Lattimer-Swesty [60] and the one of H. Shen et al. [61, 62]. Furthermore, we discuss and include in **GR1D** the deleptonization treatment of [63] for the collapse phase and a postbounce 3-flavor neutrino treatment based on the leakage schemes of [64, 65] as well as an approximate way of including neutrino heating.

Due to these approximations in the neutrino treatment, **GR1D** in its present form cannot be used for accurate simulations addressing the core-collapse supernova mechanism or neutrino-induced nucleosynthesis. However, we find that with the present treatment, **GR1D** reproduces very well qualitatively the salient features of the postbounce evolution of core-collapse supernovae as predicted by full 1D radiation-hydrodynamics simulations. Moreover, we find that **GR1D** may be used to make quantitatively reliable predictions on the time of black hole formation in failing core-collapse supernovae and on the maximum mass of the PNS.

This article is structured as follows. In section 2, we discuss our 1D GR hydrodynamics and curvature equations and their implementation in **GR1D**. Section 3 introduces the EOS provided with **GR1D** and in section 4 we detail our pre-bounce deleptonization and postbounce leakage and neutrino heating schemes. A number of code tests and example simulations are presented in section 5 and 6. We wrap up and

conclude in section 7.

We assume spacelike signature $(-, +, +, +)$ and, unless mentioned otherwise, use units of $G = c = M_\odot = 1$, but use cgs units for the microphysics and neutrino leakage/heating quantities.

2. 1D GR Hydrodynamics and Curvature Equations

2.1. Curvature Equations in 1D RGPS

We follow [30, 34] who formulate the 3+1 GR curvature and hydrodynamics equations in RGPS coordinates. In these coordinates and in spherical symmetry, the shift vector vanishes and the metric is diagonal and closely resembles the Schwarzschild metric. The invariant line element is

$$\begin{aligned} ds^2 &= g_{\mu\nu} dx^\mu dx^\nu, \\ &= -\alpha(r, t)^2 dt^2 + X(r, t)^2 dr^2 + r^2 d\Omega^2, \end{aligned} \quad (1)$$

where α and X can be written more conveniently as functions of a metric potential, $\Phi(r, t)$, and the enclosed gravitational mass $M_{\text{grav}}(r, t) = m(r, t)$,

$$\alpha(r, t) = \exp[\Phi(r, t)], \quad X(r, t) = \left(1 - \frac{2m(r, t)}{r}\right)^{-1/2}. \quad (2)$$

We assume ideal hydrodynamics for which the fluid stress-energy tensor and the matter current density are-

$$T^{\mu\nu} = \rho h u^\mu u^\nu + P g^{\mu\nu} \quad \text{and} \quad J^\mu = \rho u^\mu, \quad (3)$$

where ρ is the baryonic density, P is the fluid pressure, h is the specific enthalpy equal to $1 + \epsilon + P/\rho$ with ϵ being the specific internal energy. u^μ is the four-velocity and, in 1D without rotation, is equal to $[W/\alpha, Wv^r, 0, 0]$. $W = (1 - v^2)^{-1/2}$ is the Lorentz factor and $v = Xv^r$. The equation for the gravitational mass needed for determining the metric coefficient $X(r, t)$ of (2) is derived from the Hamiltonian constraint equation and reads

$$m(r, t) = 4\pi \int_0^r (\rho h W^2 - P + \tau_m^\nu) r'^2 dr'. \quad (4)$$

Here, τ_m^ν is the contribution to the gravitational mass from the energy and pressure of trapped neutrinos (see section 4.3). The expression for the metric potential $\Phi(r, t)$ is determined via the momentum constraints, taking into account the polar slicing condition that imposes $\text{tr} K = K_r^r$, where K_{ij} is the extrinsic curvature tensor (see [30, 35] for details). It reads,

$$\Phi(r, t) = \int_0^r X^2 \left[\frac{m(r', t)}{r'^2} + 4\pi r' (\rho h W^2 v^2 + P + \tau_\Phi^\nu) \right] dr' + \Phi_0, \quad (5)$$

where analogous to (4), τ_Φ^ν accounts for the effect of trapped neutrinos. Φ_0 is determined by matching the solution at the star's surface ($r = R_\star$) to the Schwarzschild metric,

$$\Phi(R_\star, t) = \ln[\alpha(R_\star, t)] = \frac{1}{2} \ln \left[1 - \frac{2m(R_\star, t)}{R_\star} \right]. \quad (6)$$

We use standard 2nd order methods to perform the integrals in (4) and (5) and obtain values at cell centers as well as at cell interfaces.

2.2. GR Hydrodynamics in 1D RGPS

The evolution equations for the matter fields are derived from the local conservation laws for the stress-energy tensor, $\nabla_\mu T^{\mu\nu} = 0$, and for the matter current density $\nabla_\mu J^\mu = 0$. We write the GR hydrodynamics equations along the lines of the flux-conservative Valencia formulation (e.g., [66–68]) with modifications for spherically-symmetric flows proposed by [34] and neutrino sources. Derivation details are presented in Appendix A.

We write the set of evolution equations as,

$$\partial_t \vec{U} + \frac{1}{r^2} \partial_r \left[\frac{\alpha r^2}{X} \vec{F} \right] = \vec{S}, \quad (7)$$

where \vec{U} is the set of conserved variables, \vec{F} is their flux vector, and \vec{S} is the vector containing gravitational, geometric, and neutrino-matter interaction sources and sinks. In 1D and without rotation, $\vec{U} = [D, DY_e, S^r, \tau]$. The conserved variables are functions of the primitive variables ρ, Y_e, ϵ, v , and P and are given by

$$\begin{aligned} D &= \alpha X J^t = X \rho W, \\ DY_e &= \alpha X Y_e J^t = X \rho W Y_e, \\ S^r &= \alpha X T^{tr} = \rho h W^2 v, \\ \tau &= \alpha^2 T^{tt} - D = \rho h W^2 - P - D, \end{aligned} \quad (8)$$

where Y_e is the electron fraction, the number of electrons per baryon, and the only compositional variable needed to describe matter in nuclear statistical equilibrium (NSE). Note that there is a misprint in the central part of Eq. 9 of [34] which is missing a factor of X which we have corrected here. The flux \vec{F} is given by $\vec{F} = [Dv, DY_e v, S^r v + P, S^r - Dv]$ and the sources and sinks are given by

$$\begin{aligned} \vec{S} = & \left[0, R_{Y_e}^\nu, (S^r v - \tau - D) \alpha X \left(8\pi r P + \frac{m}{r^2} \right) + \alpha P X \frac{m}{r^2} \right. \\ & \left. + \frac{2\alpha P}{Xr} + Q_{S^r}^{\nu,E} + Q_{S^r}^{\nu,M}, Q_\tau^{\nu,E} + Q_\tau^{\nu,M} \right]. \end{aligned} \quad (9)$$

The source and sink terms $R_{Y_e}^\nu, Q_{S^r}^{\nu,E}, Q_{S^r}^{\nu,M}, Q_\tau^{\nu,E}$, and $Q_\tau^{\nu,M}$ are associated with neutrinos and are discussed in section 4 and derived in Appendix A.

We use a semi-discrete approach and first discretize (7) in space, then apply the method of lines (MoL, [69]) and perform the time integration of the conserved variables via standard 2nd or 3rd order Runge-Kutta integrators with a Courant factor of 0.5.

The spatial discretization follows the finite-volume approach (e.g., [34, 68]) and all variables are defined at cell centers i and must be reconstructed (i.e., interpolated) at cell interfaces, where inter-cell fluxes are computed. This interpolation must be monotonic to ensure stability. We use the nominally 3rd order (in smooth parts of the flow) piecewise-parabolic method (PPM, [70]) to interpolate the primitive variables and then set up the conserved variables at the cell interfaces. We also implement piecewise-constant reconstruction as well as piecewise-linear (total-variation-diminishing [TVD]) reconstruction with Van Leer’s limiter [71]. The latter we use exclusively in the innermost 3 to 5 zones to avoid oscillations near the origin.

Once the variables have been reconstructed at the cell interfaces, we evaluate the physical interface fluxes $\vec{F}_{i+1/2}$ with the HLLC Riemann solver [72]. The right-hand-

side (RHS) flux update term for \vec{U}_i then reads,

$$\text{RHS}_i = -\frac{1}{r_i^2 \Delta r_i} \left[\frac{\alpha_{i+1/2} r_{i+1/2}^2}{X_{i+1/2}} \vec{F}_{i+1/2} - \frac{\alpha_{i-1/2} r_{i-1/2}^2}{X_{i-1/2}} \vec{F}_{i-1/2} \right]. \quad (10)$$

Gravitational, geometrical, and neutrino-matter interaction sources/sinks are not taken into account in the flux computation and are coupled into the MoL integration.

After the update of the conserved variables D , DY_e , S^r and τ , primitive variables ρ , Y_e , v , ϵ , and $P(\rho, \epsilon, Y_e)$ must be extracted since they are needed for the next timestep. In the general case, the primitive variables (with the exception of Y_e) cannot be expressed algebraically in terms of the conserved variables (see, e.g., [67]). Hence, we employ an iterative approach and make an initial guess using P_{old} from the previous timestep,

$$v = \frac{S^r}{\tau + D + P_{\text{old}}}, \quad \rho = \frac{D}{XW}, \quad \epsilon = \frac{\tau + D + P_{\text{old}}(1 - W^2)}{\rho W^2} - 1, \quad (11)$$

where we note that X can be calculated from the conserved variables as $\rho h W^2 - P = \tau + D$. W is calculated from the estimate of v . We then call the EOS to obtain a new pressure and iterate this process using a Newton-Raphson method until convergence (we typically stop the iteration at a fractional pressure difference of 10^{-10} between iteration steps).

2.3. Extension to 1.5D: Including Rotation

Lagrangian spherically-symmetric stellar evolution codes have long included rotation and rotational effects in an approximate fashion (e.g., [73–75]). The way this is typically done is to make the assumption that the star has constant angular velocity on spherical shells. In order to compute the effective specific centrifugal force acting on a fluid parcel, we compute the angular average of $(\vec{\omega} \times \vec{r})^2$ on a spherical shell of radius r , which leads to $f_{\text{cent}} = 2/3 \omega^2 r$. In Newtonian Lagrangian calculations, specific angular momentum $j = \omega r^2$ is conserved by construction and the effective centrifugal force appears in the momentum equation. Relatively recently, such an approach has also been taken in the Newtonian 1D core collapse calculations of [76, 77] in order to take into account the effect of rotation approximately. In the Eulerian frame and in GR the situation is more complicated. We must solve an equation for angular momentum conservation on top of taking into account a centrifugal force term in the momentum equation. We begin by defining an azimuthal Eulerian velocity $v^\phi (= \omega)$ and, in order to obtain a quantity of dimension velocity, we also define $v_\phi = r v^\phi$ (note that $u^\phi = W v_\phi / r$). With finite v^ϕ , $T^{r\phi}$ is finite and W becomes $W = (1 - v^2 - 2/3 v_\phi^2)^{-1/2}$ in our effective approach. We provide derivation details in Appendix A.2 and present here only the results. The modified stress-energy tensor leads to an additional equation for angular momentum conservation analogous to (7),

$$\partial_t(S_\phi) + \frac{1}{r^2} \partial_r \left(\frac{\alpha r^2}{X} F_\phi \right) = S_\phi, \quad (12)$$

where

$$\begin{aligned} S_\phi &= \rho h W^2 v_\phi r, \\ F_\phi &= \rho h W^2 v_\phi r v = S_\phi v, \\ S_\phi &= \rho h W^2 \alpha v v_\phi X \left[4\pi r^2 P + \frac{m}{r} \right]. \end{aligned} \quad (13)$$

Also, an additional term, accounting for the centrifugal force,

$$+ \alpha \frac{2}{3} \left(\frac{\rho h W^2 v_\varphi^2}{X r} \right) , \quad (14)$$

appears on the RHS of the equation for S^r . Finally, the change of the stress-energy tensor also has an effect on the metric potential Φ , whose equation is now given by

$$\partial_r \Phi = X^2 \left[\frac{m}{r^2} + 4\pi r \left(\rho h W^2 (v^2 + \frac{2}{3} v_\varphi^2) + P + \tau_\Phi^\nu \right) \right] . \quad (15)$$

We implement this 1.5D treatment of rotation in **GR1D**, but keep the metric diagonal. The 1.5D treatment should be rather accurate for slow rotation, and, as shown by [77], will still capture qualitatively the effect of centrifugal support due to rapid rotation. For completeness, we note that the total angular momentum of the system (see, e.g., [78]) is given by,

$$J = \int_0^\infty T_\phi^t \sqrt{-g} d^3x = \frac{8\pi}{3} \int_0^\infty \rho h X W^2 r v_\varphi r^2 dr , \quad (16)$$

where we include a factor of 2/3 to account for the angular average. The rotation parameter β , defined as the ratio $T/|W_{\text{grav}}|$ of rotational kinetic to gravitational energy is

$$T/|W_{\text{grav}}| = \frac{T}{|M_{\text{grav}} - M_{\text{proper}} - T|} , \quad (17)$$

where

$$T = \frac{1}{2} \int_0^\infty \omega T_\phi^t \sqrt{-g} d^3x = \frac{4\pi}{3} \int_0^\infty \rho h X W^2 v_\varphi^2 r^2 dr , \quad (18)$$

where again a factor of 2/3 in the last step is from performing an angular average. M_{proper} is given by,

$$M_{\text{proper}} = 4\pi \int_0^\infty (\rho + \rho\epsilon) X W r^2 dr , \quad (19)$$

and M_{grav} is specified by (4).

3. Equations of State (EOS)

An EOS is needed to close the system of GR hydrodynamics equations and provide the pressure as well as other thermodynamic quantities as a function of density, temperature (or specific internal energy), and composition. In **GR1D**, we include for test simulations the standard analytic polytropic (isentropic “cold”, $P = K\rho^\Gamma$) and the Γ -law EOS (“hot”, $P = (\Gamma - 1)\rho\epsilon$). These are inappropriate for stellar collapse since they do not capture the stiffening of the EOS at nuclear density. An analytic EOS, able to capture this effect qualitatively and include nonisentropic effects, is the *hybrid* EOS [79] which we include in **GR1D** and discuss in section 3.1. For a more realistic description of the thermodynamics of nuclear matter, an EOS built from a microphysical finite-temperature model for nuclear matter is needed. This is also a prerequisite for any kind of neutrino treatment, since crucial compositional information as well as chemical potentials must be derived from a microphysical model. Such microphysical EOS are too complicated to be computed on the fly in a simulation and

are used in tabulated form with interpolation. GR1D is able to handle such EOS and we provide tables at <http://www.stellarcollapse.org/microphysics> for the EOS of Lattimer & Swesty ([60], LS EOS) and for the one of H. Shen et al. ([61, 62], HShen EOS). The details of these tables and the routines facilitating their use are discussed in sections 3.2 and 3.3.

3.1. Hybrid EOS

The hybrid EOS found widespread use in early multi-D simulations of rotating core collapse (e.g., [48, 80]), but was shown by [52, 53] to lead in some cases to qualitatively incorrect results for the collapse dynamics and the resulting gravitational wave signal. We include it in GR1D, because its analytic nature provides for very fast calculations, allowing us to readily test the GR hydrodynamics of GR1D.

The hybrid EOS splits the pressure into a polytropic (cold) and a thermal component,

$$P = P_{\text{cold}} + P_{\text{thermal}} . \quad (20)$$

The cold part is piecewise polytropic. It is composed of a polytropic EOS with $\Gamma = \Gamma_1$ for densities below nuclear (ρ_{nuc}) and another polytropic EOS with $\Gamma = \Gamma_2$ for densities above ρ_{nuc} . The two are smoothly matched at ρ_{nuc} which makes the polytropic constant K_2 of the high-density part a function of the two Γ s, of K_1 , and of the transition density ρ_{nuc} (see, e.g. [79–81] for a description of the procedure and detailed expressions). The thermal part is modeled via a Γ -law with Γ_{th} . It becomes relevant only after core bounce when shocks are present, making the flow nonadiabatic. Its contribution is determined via the thermal specific internal energy which is the difference between the primitive variable ϵ and the cold specific internal energy, $\epsilon_{\text{th}} = \epsilon - \epsilon_{\text{cold}}$.

For collapse simulations, we set $K_1 = 1.2435 \times 10^{15} (Y_e)^{4/3} [\text{cgs}]$ (the value appropriate for a relativistic degenerate gas of electrons, [80, 82]) with $Y_e = 0.5$. We choose a value below, but close to $4/3$ for Γ_1 and typically set $\Gamma_2 = 2.5$ to mimic the stiff nuclear EOS above ρ_{nuc} which we set to $2 \times 10^{14} \text{ g cm}^{-3}$. Γ_{th} we normally keep at 1.5 to model a mixture of relativistic ($\Gamma = 4/3$) and nonrelativistic ($\Gamma = 5/3$) thermal contributions. This leads to rapid shock propagation and explosion. When simulating BH formation with the hybrid EOS, we set Γ_{th} to smaller values. This reduces the postshock thermal pressure and leads to shock stagnation.

3.2. Lattimer-Swesty EOS

The LS EOS [60] is derived from a finite-temperature compressible liquid-droplet model [83] with a Skyrme nuclear force, uses the single heavy nucleus approximation, and assumes nuclear statistical equilibrium (NSE). NSE holds at $T \gtrsim 0.5 \text{ MeV}$ which in core collapse and supernova matter is typically the case at $\rho \gtrsim \text{few} \times 10^7 \text{ g cm}^{-3}$.

The LS EOS routines are open source and available from the Stony Brook group[‡]. We employ their baryonic parts to generate tables with nuclear incompressibilities K_0 of 180 MeV, 220 MeV, and 375 MeV (the larger K_0 , the stiffer the nuclear EOS). Hereafter, we refer to these K_0 -variants of the LS EOS as LS180, LS220, and LS375. The symmetry energy S_v is set in all variants to 29.3 MeV for all K_0 . Electrons and photons are added using the routines provided by Timmes’s EOS§ [84].

[‡] <http://www.astro.sunysb.edu/dswesty/lseos.html>

[§] http://cococubed.asu.edu/code_pages/eos.shtml

We compute the maximum cold neutron star masses for the three LS EOS variants by setting $T = 0.1 \text{ MeV}$ and assuming neutrino-less β -equilibrium. The results are $1.83 M_\odot$ ($2.13 M_\odot$), $2.04 M_\odot$ ($2.41 M_\odot$), $2.72 M_\odot$ ($3.35 M_\odot$) for gravitational (baryonic) mass and for $K_0 = 180 \text{ MeV}$, $K_0 = 220 \text{ MeV}$, and $K_0 = 375 \text{ MeV}$, respectively. The coordinate radii of these maximum mass stars are 10.1 km , 10.6 km , and 12.3 km .

Our LS EOS tables have 18 evenly-spaced points per decade in $\log_{10} \rho$ ranging from $10^3 - 10^{16} \text{ g cm}^{-3}$, 30 points per decade in $\log_{10} T$ ranging from $10^{-2} - 10^{2.4} \text{ MeV}$, and 50 points equally spaced in electron fraction from 0.035 to 0.53. This table resolution is sufficiently good to allow the use of simple and fast tri-linear interpolation (in $\log_{10}(\rho)$, $\log_{10}(T)$, Y_e), in collapse simulations while maintaining good thermodynamic consistency. In tests of adiabatic collapse, the inner-core entropy is conserved to $\sim 1\%$ from the onset of collapse to core bounce.

To generate the LS EOS tables, we employ the LS EOS at densities above 10^8 g cm^{-3} , but, due to unreliable convergence, use linear extrapolation of the Helmholtz free energy F in Y_e for $Y_e > 0.5$ and in T at $T < 0.06 \text{ MeV}$. Note that the latter is far away from NSE, but is never reached by core collapse trajectories at $\rho > 10^8 \text{ g cm}^{-3}$. At densities below 10^8 g cm^{-3} , we use the Timmes EOS [84] and assume that the matter is an ideal gas composed of electrons, photons, neutrons, protons, alpha particles, and heavy nuclei with the average A and Z given by the LS EOS at the transition.

Since the specific internal energies returned by the baryonic part of the Timmes EOS do not contain the nuclear binding energy, we shift the zero point of the Timmes EOS so that the returned specific internal energies are consistent with the LS EOS values at the transition point. For simplicity, we keep baryonic compositional variables fixed at the values obtained from the LS EOS at the transition density. These particular choices for the baryonic component have little effect at low densities where the thermodynamics are dominated by electrons at low to intermediate temperatures and by photons at high temperatures. However, for full core-collapse supernova simulations that intend to address also nuclear burning and nucleosynthesis aspects, a more involved consistent NSE/non-NSE EOS treatment involving the advection of many chemical species and a treatment of their interactions with a nuclear reaction network is necessary. We will leave such a treatment to future work (but see, e.g., [57, 85] for discussions of such implementations).

When using finite-temperature microphysical NSE EOS such as the LS EOS in GR hydrodynamics codes, two additional caveats need to be taken into account: (1) The thermodynamic potential from which all dependent variables are derived is the Helmholtz free energy F . This makes the EOS a function of $\{\rho, T, Y_e\}$ while GR hydrodynamics codes such as **GR1D** operate on the primitive thermodynamic and compositional variables $\{\rho, \epsilon, Y_e\}$. Hence, in a typical EOS call it is first necessary to determine $T(\rho, \epsilon, Y_e)$ through a root-finding procedure, before the dependent variables can be obtained through tri-linear interpolation in $\{\rho, T, Y_e\}$. (2) In contrast to Newtonian hydrodynamics that involves only differences of the specific internal energy ϵ , GR codes depend directly on ϵ through its contribution to the matter stress-energy tensor. Hence, it is important to find and use a physically correct energy zero point and ensure that there are no rest-mass contributions included in ϵ .

3.3. HShen EOS

The HShen EOS [61, 62] is based on a relativistic mean-field model for nuclear interactions, assumes NSE, and is extended with the Thomas-Fermi approximation to describe the homogeneous phase of matter as well as the inhomogeneous matter composition. K_0 of the HShen EOS is 281 MeV and the symmetry energy S_v has a value of 36.9 MeV. The authors of the HShen EOS provide the baryonic component^{||} in tabulated form only. The provided table is not uniformly spaced and has too low resolution to be used directly with fast tri-linear interpolation in simulations. Hence, we generate a finer uniformly-spaced table that has 18 points per decade in $\log_{10} \rho$ from $10^3 - 10^{15.36} \text{ g cm}^{-3}$, 41 points per decade in $\log_{10} T$ from $10^{-2} - 10^{2.4} \text{ MeV}$, and 50 points in Y_e covering the interval $0.015 - 0.56$. We interpolate all dependent variables from the original HShen table using the cubic Hermite interpolation function given in [86] modified to have monotonic interpolation behavior according to the prescription of [87]. The interpolation is performed first bicubic in ρ, T , then cubic in Y_e . Alternatively to the just described, one could interpolate the Helmholtz free energy F and re-derive dependent variables by taking derivatives of F on the interpolated table (see, e.g., [86]). We decided against this approach, since it would require quintic interpolation and the knowledge of the second derivatives of F at each point in the original table, some of which would have to be computed by taking second derivatives in the coarse original table. Also, compositional information cannot be obtained directly from F and would have to be interpolated from the original table.

We perform the described interpolation at densities above 10^7 g cm^{-3} . For points with $T > 100 \text{ MeV}$ and $T < 0.1 \text{ MeV}$ we extrapolate most variables linearly, keeping only the compositions fixed. We add photons and electrons after interpolation using the routines of the Timmes EOS. At densities below 10^7 g cm^{-3} , we employ the Timmes EOS in the same fashion as described in the above for the LS EOS.

We compute the maximum cold neutron star masses for the HShen EOS in the same way as for the LS EOS and find $2.24 M_\odot$ and $2.61 M_\odot$, for the gravitational and baryonic value, respectively. The coordinate radius of the corresponding star is 12.6 km.

4. Neutrino Leakage and Heating

4.1. Deleptonization and Electron Capture in the Collapse Phase

Electron capture on free and bound protons leads to the emission of neutrinos that stream away from the core and carry away net lepton number at densities below $\sim 10^{12} \text{ g cm}^{-3}$. Hence, one speaks of the deleptonization of the core. The change of the electron fraction Y_e in the collapse phase due to deleptonization has important dynamical consequences. A reduction of Y_e leads to a decrease of the mass of the homologously collapsing inner core whose kinetic energy is initially imparted on the supernova shock and which turns into the PNS core after bounce [1]. We take electron capture in collapse into account in GR1D with the approximate scheme of Liebendörfer [63] who observed that Y_e of infalling mass elements depends primarily on the local matter density ρ and can be parameterized with rather high precision on the basis of radiation-hydrodynamic calculations.

^{||} <http://user.numazu-ct.ac.jp/~sumi/eos>

Operator-split, after a hydrodynamics update, we compute the change in Y_e ,

$$\Delta Y_e = \min [0, \bar{Y}_e(\rho) - Y_e] , \quad (21)$$

which ensures for consistency that a change in Y_e is either negative or 0. We use for $\bar{Y}_e(\rho)$ the fitting formula given in [63] with parameters $\rho_1 = 3 \times 10^7 \text{ g cm}^{-3}$, $\rho_2 = 2 \times 10^{13} \text{ g cm}^{-3}$, $Y_1 = 0.5$, $Y_2 = 0.278$, and $Y_c = 0.035$ corresponding to the $15-M_\odot$ model of [88], evolved as model G15 by [2]. **GR1D** also contains an interpolation routine to use numerical $\bar{Y}_e(\rho)$ data.

Electron capture leads to a change in the entropy (s , the specific entropy in units of k_B /baryon) that is carried away by neutrinos leaving the core at densities below an assumed trapping density $\rho_{\text{trap}} = 2 \times 10^{12} \text{ g cm}^{-3}$. The entropy change is given by

$$\Delta s = -\Delta Y_e \frac{\mu_p - \mu_n + \mu_e - E_\nu}{k_B T} . \quad (22)$$

E_ν is the energy of the escaping neutrinos (set to 10 MeV). μ_p , μ_n , and μ_e are the proton, neutron, and electron chemical potentials including rest mass, respectively. Following [63], we set $\Delta s = 0$ if $\mu_p + \mu_n + \mu_e < E_\nu$ and above ρ_{trap} . After updating the entropy, we use the EOS to update the specific internal energy ϵ for consistency with the new Y_e and s .

We employ the outlined deleptonization scheme until core bounce (defined as the time when the peak entropy of the inner core surpasses $3 k_B$ /baryon) and until 5ms after bounce for yet unshocked regions of the outer core that will settle in the high-density outer PNS and only in this way assume realistic postbounce Y_e .

4.2. Postbounce Deleptonization and Neutrino Heating/Cooling

At core bounce a strong hydrodynamic shock wave is generated that travels outward into the outer core, heating and dissociating infalling heavy nuclei into nucleons. Electron capture occurs rapidly on free protons and a sea of electron neutrinos (ν_e) builds up and is released in the ν_e burst when the shock breaks through the neutrinosphere[¶], deleptonizing the postshock region and leaving behind a “trough” in the Y_e profile (e.g., [41]). The softening of the EOS due to dissociation of nuclei and postshock energy loss to escaping neutrinos lead the shock to stall and turn into an accretion shock soon after bounce. In the hot postshock region, electrons are less degenerate and positrons appear and are captured on neutrons, leading to a rise of the $\bar{\nu}_e$ luminosity. In addition, in the PNS and in the postshock region, neutrinos and antineutrinos of all flavors are emitted by thermal processes.

The simple $\bar{Y}_e(\rho)$ parameterization discussed in the previous section 4.1 is not adequate to capture these effects and, in principle, a full neutrino energy-dependent radiation-hydrodynamics treatment would be needed for accurately capturing postbounce neutrino effects. Such a treatment may be added in future versions of **GR1D**. In the present version of **GR1D**, we approximate postbounce neutrino transport by a gray (energy-averaged) neutrino leakage scheme augmented with a simple prescription for neutrino heating in the postshock region. This approach captures the most important qualitative aspects of the postbounce evolution well and, as we demonstrate in section 6.2, is sufficiently quantitatively accurate to make

[¶] The neutrinosphere is the effective “decoupling” surface of neutrinos where the optical depth τ_ν of the supernova matter is $2/3$. Its position depends strongly on neutrino energy.

reliable predictions of the time of BH formation and the maximum PNS mass in failing core-collapse supernovae.

Our implementation in **GR1D** combines elements of the neutrino leakage schemes of Ruffert et al. [64] and of Rosswog & Liebendörfer [65]. We consider three neutrino species, ν_e , $\bar{\nu}_e$, and ν_x . In the latter, we lump together μ and τ neutrinos and anti-neutrinos since they interact only by neutral-current processes in the core collapse context and have very similar cross sections. The mean (energy-averaged) optical depth is

$$\tau_{\nu_i}(r) = \int_r^\infty \kappa_t(\nu_i) X dr, \quad (23)$$

where $\kappa_t(\nu_i)$ is the mean transport opacity equal to the sum of absorptive and scattering opacities⁺ for neutrino species ν_i . We follow [64] in the calculation of $\kappa_t(\nu_i)$ and of the approximate neutrino degeneracy parameters ($\eta_{\nu_i} = \mu_{\nu_i}/T$). We consider opacity contributions from neutrino scattering on neutrons, protons, and heavy nuclei and absorption of neutrinos (anti-neutrinos) on neutrons (protons). For heavy-lepton neutrinos that are never degenerate, we set $\eta_{\nu_x} = 0$. η_{ν_e} is known (1) in β -equilibrium where $\eta_{\nu_e}^{\text{eq}} = \eta_e + \eta_p - \eta_n$ (where we assume that the chemical potentials include rest mass terms) and (2) in the free streaming limit, where $\eta_{\nu_e}^{\text{stream}} = 0$. Furthermore, $\eta_{\bar{\nu}_e}^{\text{eq}} = -\eta_{\nu_e}^{\text{eq}}$. In between the two regimes, the neutrino distribution function cannot be derived from first principles and neutrino transport is necessary for a correct estimate of η_{ν_e} and $\eta_{\bar{\nu}_e}$. As an approximation, we interpolate between (1) and (2) using the optical depth,

$$\eta_{\nu_i} = \eta_{\nu_i}^{\text{eq}}(1 - e^{-\tau_{\nu_i}(\eta_{\nu_i})}). \quad (24)$$

Note that τ_{ν_i} depends on η_{ν_i} and vice versa. Hence, we iterate their calculation until convergence is reached*.

Knowing τ_{ν_i} and η_{ν_i} , we use the leakage scheme of [65] to calculate the neutrino emission rates for the capture processes $p + e^- \rightarrow \nu_e + n$ and $e^+ + n \rightarrow \bar{\nu}_e + p$ and thermal emission via electron-positron annihilation and plasmon decay to $\nu\bar{\nu}$ pairs. We modify the scheme of [65] in the following ways: (i) we use the interpolated η_{ν_i} from above instead of the equilibrium values suggested in [65], (ii) we increase their diffusion time scale $t_{\nu_i}^{\text{diff}}$ by a factor of 2 to obtain more reasonable neutrino luminosity predictions, and (iii) for simplicity, we use the analytic thermal emissivities from [64]. Following [65], we then interpolate the effective volumetric energy loss $Q_{\text{eff}}^{\text{leak}}$ (erg/cm³/s) and effective number loss $R_{\text{eff}}^{\text{leak}}$ (#/cm³/s) between the limits of diffusive emission (subscript “diff”) and free emission (subscript “loc”) using

$$\chi_{\text{eff},\nu_i}^{\text{leak}} = \chi_{\text{loc},\nu_i}^{\text{leak}} / (1 + \chi_{\text{loc},\nu_i}^{\text{leak}} / \chi_{\text{diff},\nu_i}^{\text{leak}}), \quad (25)$$

where $\chi = Q$ for energy loss and $\chi = R$ for number loss (see [65] for definitions and details). We define the neutrino luminosity seen by an observer at rest at radius r in the coordinate frame by summing up the effective energy emission rates from each

⁺ Note that the opacities for neutrino number and neutrino energy transport differ. Hence, the optical depths for number and energy transport must be computed separately [64]. We neglect this subtlety and use the optical depths for energy transport throughout **GR1D**.

* Initially we choose $\kappa_{\nu_i}(r) = 10^{-5} \text{cm}^{-1}$ determine τ_{ν_i} through (23) and iterate (24). For all subsequent times we use the previously determined value of τ_{ν_i} as a starting point, convergence (fractional difference in $\kappa_{\nu_i} < 10^{-10}$) is typically reached after three iterations.

zone interior to r , transforming from the fluid rest frame (FRF) to the coordinate frame (CF), and applying the redshift (see Appendix B for details),

$$L_{\nu_i}^{\text{CF}}(r) = 4\pi \int_0^r \left[\frac{\alpha(r')}{\alpha(r)} \right] Q_{\text{eff},\nu_i}(r') [\alpha(r')W(r')(1+v(r'))] X(r') r'^2 dr' . \quad (26)$$

For an observer at rest at $r = \infty$ ($\alpha(\infty) = 1$),

$$L_{\nu_i}(\infty) = 4\pi \int_0^\infty \alpha(r') Q_{\text{eff},\nu_i}(r') [\alpha(r')W(r')(1+v(r'))] X(r') r'^2 dr' . \quad (27)$$

It is useful to note the neutrino luminosity as seen by an observer at rest in the fluid rest frame at radius r ,

$$L_{\nu_i}^{\text{FRF}}(r) = \frac{L_{\nu_i}^{\text{CF}}(r)}{\alpha(r)W(r)(1+v(r))} , \quad (28)$$

where the denominator transforms the luminosity from the frame of an observer at rest in the coordinate frame (26) to the fluid rest frame.

4.2.1. Neutrino Heating. In addition to the above leakage scheme, we include a parameterized heating scheme to mimic neutrino absorption in the postshock region. Heating occurs at intermediate to low optical depths where neutrinos begin to decouple from matter and a net energy transfer from neutrinos to the fluid is possible (see, e.g., [89]). The dominant heating processes are the charged-current capture reactions of ν_e on neutrons and $\bar{\nu}_e$ on protons. We take the absorption cross sections from [65],

$$\sigma_{\text{heat},\nu_e} = \frac{(1+3g_A^2)}{4} \sigma_0 \frac{\langle \epsilon^2 \rangle_{\nu_e}^{\text{ns}}}{(m_e c^2)^2} \langle 1 - f_{e^-} \rangle , \quad (29)$$

$$\sigma_{\text{heat},\bar{\nu}_e} = \frac{(1+3g_A^2)}{4} \sigma_0 \frac{\langle \epsilon^2 \rangle_{\bar{\nu}_e}^{\text{ns}}}{(m_e c^2)^2} \langle 1 - f_{e^+} \rangle , \quad (30)$$

where σ_0 is a reference weak-interaction cross section equal to $1.76 \times 10^{-44} \text{ cm}^2$, $g_A \sim -1.25$, and the Fermi blocking factors $\langle 1 - f_i \rangle$ are defined analogously to [64, 65]. In the postshock region the positron blocking term is negligible but the electron blocking term can be significant around the time of bounce. Following [89], we set the mean squared neutrino energy to $\langle \epsilon^2 \rangle_{\nu_i}^{\text{ns}} = T(\tau_{\nu_i} = \frac{2}{3})^2 \mathcal{F}_5(\eta_{\nu_i}^{\text{ns}}) / \mathcal{F}_3(\eta_{\nu_i}^{\text{ns}})$, where $T(\tau_{\nu_i} = \frac{2}{3})$ is the temperature at the neutrinosphere of species i , superscript ns denotes neutrinospheric values, and $\mathcal{F}_n(\eta) = \int_0^\infty \frac{x^n dx}{\exp(x-\eta)+1}$ is the n^{th} Fermi integral (we approximate Fermi integrals via the formulae given in [90]).

Given the neutrino luminosity $L_{\nu_i}^{\text{FRF}}(r)$ obtained from the leakage scheme (28), we write the local neutrino heating rate in units of $\text{erg cm}^{-3} \text{ s}^{-1}$ as

$$Q_{\nu_i}^{\text{heat}}(r) = f_{\text{heat}} \frac{L_{\nu_i}^{\text{FRF}}(r)}{4\pi r^2} \sigma_{\text{heat},\nu_i} \frac{\rho}{m_u} X_i \left\langle \frac{1}{F_{\nu_i}} \right\rangle e^{-2\tau_{\nu_i}} , \quad (31)$$

where m_u is atomic mass unit and the mass fraction $X_i = X_n$ in the case of ν_e absorption and $X_i = X_p$ for $\bar{\nu}_e$ s. $\langle 1/F_{\nu_i} \rangle$ is the mean inverse flux factor describing the degree of forward-peaking of the radiation field (e.g., [44, 89]; $\langle 1/F_{\nu_i} \rangle$ is 1 for free streaming and diverges at high optical depth). We estimate $\langle 1/F_{\nu_i} \rangle$ by the interpolation $\langle 1/F_{\nu_i}(\tau) \rangle = 4.275\tau + 1.15$, which reproduces the predicted values of 4 at the neutrinosphere [89] and levels off at a value of 1.15 at low optical depth in the outer postshock region. We choose the latter value instead of 1, because (a) the

radiation field becomes fully forward peaked only outside the shock (e.g., [44]), and (b) the linear interpolation in τ drops off too quickly compared to full simulations [44], hence the higher floor value to compensate. Finally, we introduce the attenuation factor $e^{-2\tau_{\nu_i}}$ to cut off heating near and below the neutrinosphere and the scaling factor f_{heat} to allow for an ad-hoc increase of the heating rate. Once the heating rate for a computational cell is computed, we reduce the outgoing luminosity by the deposited power for overall energy conservation. In the coordinate frame (26) now becomes,

$$L_{\nu_i}^{\text{CF}}(r) = 4\pi \int_0^r \left[\frac{\alpha(r')}{\alpha(r)} \right] [Q_{\text{eff},\nu_i}(r') - Q_{\nu_i}^{\text{heat}}(r')] [\alpha(r')W(r')(1+v(r'))] X(r')r'^2 dr' . \quad (32)$$

Along with the energy deposition goes a change in Y_e which can be written as

$$R_{Y_e}^{\text{heat}} = \frac{Q_{\nu_e}^{\text{heat}}}{\langle \epsilon_{\nu_e}^{\text{ns}} \rangle} - \frac{Q_{\bar{\nu}_e}^{\text{heat}}}{\langle \epsilon_{\bar{\nu}_e}^{\text{ns}} \rangle} , \quad (33)$$

where we approximate the mean neutrino energies based on their neutrinospheric values as $\langle \epsilon_{\nu_i}^{\text{ns}} \rangle = T(\tau_{\nu_e} = \frac{2}{3})\mathcal{F}_5(\eta_{\nu_i}^{\text{ns}})/\mathcal{F}_4(\eta_{\nu_i}^{\text{ns}})$ [65].

To caution the reader, we point out that the simple gray heating scheme presented in the above is not self-consistent and cannot replace a radiation transport treatment that allows emission and absorption to balance. While we find that the combination of gray leakage/heating reproduces the overall qualitative dynamical features observed in postbounce radiation-hydrodynamic simulations, quantitative aspects are not captured as well. This is true in particular in highly dynamical situations shortly after bounce when we observe an unphysical rise of the electron fraction due to heating in the lower postshock region.

We couple the neutrino leakage/heating scheme with the GR hydrodynamics in **GR1D** through source/sink terms on the RHS of the GR hydrodynamics equations in MoL. Neutrino-matter interactions occur in the fluid rest frame where the total energy and number changes are given by

$$Q_E^0 = Q_{\text{total}}^{\text{heat}} - Q_{\text{eff,total}}^{\text{leak}} , \quad R_{Y_e}^0 = R_{\text{total}}^{\text{heat}} + R_{\text{eff,total}}^{\text{leak}} , \quad (34)$$

where $Q_{\text{total}}^{\text{heat}}$ and $Q_{\text{eff,total}}^{\text{leak}}$ are always positive or zero and $R_{\text{total}}^{\text{heat}}$ and $R_{\text{eff,total}}^{\text{leak}}$ may be positive or negative. Following [40, 56], transforming these terms to the coordinate frame via the methods laid out in Appendix A, we obtain the neutrino heating/cooling and deleptonization source/sink terms for the RHS in the MoL integration,

$$R_{Y_e}^\nu = \alpha X R_{Y_e}^0 , \quad Q_{S^r}^{\nu,E} = \alpha v W Q_E^0 , \quad Q_\tau^{\nu,E} = \alpha W Q_E^0 . \quad (35)$$

4.3. Neutrino Pressure

Electron neutrinos above trapping density in the inner core during the final phases of collapse and in the postbounce PNS contribute to both the pressure and the specific energy density (with relative importance of up to $\sim 10\%$ around core bounce [91]). We neglect neutrino contributions to pressure and energy below ρ_{trap} where they are small, but otherwise follow [63] and assume electron neutrinos and antineutrinos to be a perfect Fermi gas. The pressure is then given by

$$P_\nu = \frac{4\pi}{3(hc)^3} T^4 [F_3(\eta_\nu) + F_3(-\eta_\nu)] , \quad (36)$$

where $\eta_\nu = \mu_\nu/T$ and $\mu_\nu = \mu_e - \mu_n + \mu_p$, where the chemical potentials include rest mass contributions. F_3 is the 3rd Fermi integral which we approximate following [92]. The specific internal energy of a relativistic Fermi gas of neutrinos is simply $\epsilon_\nu = 3P_\nu/\rho$.

We treat neutrinos and fluid separately from each other and treat momentum transfer between the neutrino radiation field and the fluid approximately using the radial gradient of the neutrino pressure as suggested by [63]. We couple this radiation stress into GR1D's MoL integration of the GR momentum (S^r) and energy (τ) equations via source terms (see Appendix A for a derivation; we neglect rotational effects in these source terms),

$$Q_{S^r}^{\nu,M} = -\alpha W \frac{\partial P_\nu}{\partial r} , \quad Q_\tau^{\nu,M} = -\alpha W v \frac{\partial P_\nu}{\partial r} . \quad (37)$$

In addition to the force on the fluid due to the neutrino pressure gradient, we take into account the energy and “pressure” of the neutrino radiation field by adding P_ν and ϵ_ν through the terms τ_m^ν and τ_Φ^ν in (4) and Eqs. (5) and (15). These contributions are derived by modifying the stress-energy tensor,

$$T^{\alpha\beta} = \rho \left[1 + (\epsilon + \epsilon_\nu) + \left(\frac{P + P_\nu}{\rho} \right) \right] u^\alpha u^\beta + g^{\alpha\beta} (P + P_\nu) , \quad (38)$$

τ_m^ν and τ_Φ^ν are then given by [35]

$$\tau_m^\nu = \rho W^2 (\epsilon_\nu + P_\nu/\rho) - P_\nu = (4W^2 - 1)P_\nu , \quad (39)$$

$$\tau_\Phi^\nu = \rho W^2 v^2 (\epsilon_\nu + P_\nu/\rho) + P_\nu = (4W^2 v^2 + 1)P_\nu . \quad (40)$$

We note that if rotation is included, v^2 in (40) is replaced with $v^2 + \frac{2}{3}v_\varphi^2$.

5. Code Tests

In the following, we provide results from a set of standard and stringent relativistic hydrodynamics code tests for which analytic results exist. These involve two planar shocktube problems in section 5.1, the spherical Sedov blast wave problem in section 5.2, and Oppenheimer-Snyder collapse in section 5.3. Finally, in section 5.4, we present results from a collapse simulation of a $n = 3$ polytrope and demonstrate convergence of the hydrodynamics scheme in GR1D. With this selection, we test a broad range of aspects of potential problems to be addressed with GR1D: special relativistic effects, geometrical effects, and fully general-relativistic collapse dynamics.

5.1. Relativistic Shocktube

We assume flat space and planar geometry and perform the two relativistic shocktube tests proposed by [93]. We use a Γ -law EOS with $\Gamma = 5/3$ and a grid of length 1 with a cell spacing of $dx = 0.001$. The starting values of the density, pressure and velocity are summarized in Table 1. The left panel of figure 1 shows the exact results for velocity, density, and pressure of the mildly-relativistic problem #1 at $t = 0.4$. Superposed are the numerical results obtained with GR1D that reproduce the exact results nearly perfectly. Problem #2 is a more stringent test and involves Lorentz factors of up to 6 in the forward propagating shock and a very thin shell of trailing matter. As shown in the right panel of section 1, GR1D reproduces the exact solution

P1		P2	
$r < 0.5$	$r > 0.5$	$r < 0.5$	$r > 0.5$
$\rho = 10$	$\rho = 1$	$\rho = 1$	$\rho = 1$
$P = 13.33$	$P = 0$	$P = 10^3$	$P = 0.01$
$v = 0$	$v = 0$	$v = 0$	$v = 0$

Table 1. Initial conditions for two relativistic shocktube problems as presented in [93].

at $t = 0.4$ very well almost everywhere, but fails to completely resolve the thin shell of relativistic matter. This is most likely due to the rather diffusive nature of the HLLE Riemann solver employed in **GR1D** (see, e.g., [91, 94] for comparable results obtained with a nominally more accurate scheme). In an attempt to obtain results closer to the analytic solution we use 3rd order Runge-Kutta time integration for this test case. These deviations are not worrying since the shocks that obtain in stellar collapse are much less relativistic than that of problem #2. If **GR1D** were to be applied to ultrarelativistic outflows (e.g., in a GRB), a more precise treatment of the Riemann problem would likely be necessary.

5.2. Sedov Blast Wave

The above shocktube tests demonstrated the ability of **GR1D** to capture shocks and solve the special-relativistic hydrodynamic equations in planar geometry. Here we go back to Newtonian hydrodynamics and test instead spherical hydrodynamics with Sedov’s blast wave problem [95]. For a comparison with a large number of hydrodynamics codes, we use the initial conditions of [96]. The grid setup is

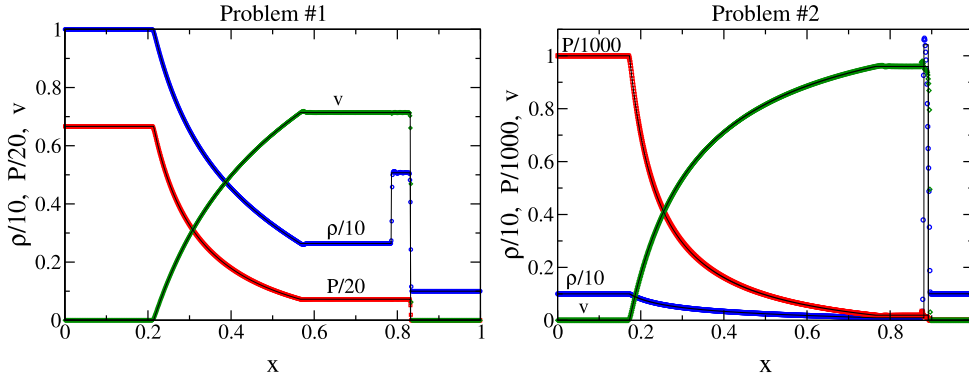


Figure 1. Relativistic shocktube simulations: Initial conditions taken from [93] and provided in Table 1. The pressure, density, and velocity are shown at $t = 0.4$ for problem #1 (left panel) and problem #2 (right panel). For reference, in both figures the pressure is denoted by boxes (red), density by circles (blue) and velocity by diamonds (green). The analytic solution is denoted by the solid line. Both problems were run with a Courant factor of 0.5 and 3rd order Runge-Kutta integration.

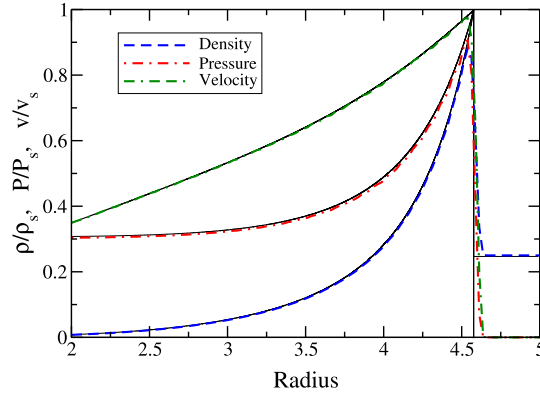


Figure 2. The Sedov blast wave problem and exact solution at $t = 0.1$. Shown are the numerical results with the exact solution underlying the various curves of density, pressure and velocity. Both the exact solution and the numerical result are normalized to the analytic value at the shock. $\rho_s = 4$, $P_s = 252.255$ and $v_s = 13.757$.

in spherical geometry with (dimensionless) $r_{max} = 10$ and $N = 400$ cells which corresponds to the maximum mesh refinement level used in [96]. We deposit a constant specific internal energy into a sphere of radius $r = 0.0875$, corresponding to a total (dimensionless) energy of $E_o = 10^5$, into a background medium of (dimensionless) $\rho_0 = 1$. We set the background energy density to an insignificant amount and use a Γ -law EOS with $\Gamma = 5/3$. Figure 2 depicts the comparison of our numerical solution with the exact result for density, velocity and pressure at $t = 0.1$ normalized in such a way that the value of all variables at the shock is 1. GR1D performs very well in the region behind the shock and provides an adequate, though not perfect, solution near the shock.

In addition to the Newtonian Sedov blast wave problem, we have also considered its relativistic variant discussed in [97]. These authors used 17 levels of adaptive mesh refinement (AMR) and we find that the lack of AMR in GR1D makes it computationally impossible to adequately resolve the relativistic Sedov problem. This, however, is not a problem for the application of GR1D to the stellar collapse problem, since the shocks appearing there are only mildly relativistic.

5.3. Oppenheimer-Snyder Collapse

For the final test problem for which an exact solution exists, we perform a simulation of the Oppenheimer-Snyder collapse (OSC) [98] of a constant-density sphere of pressureless ($P = 0$) dust. The exact solution of OSC in RGPS spacetime has been laid out by [99, 100]. We choose $M = M_\odot$, $R_\star = 10M_\odot$. We perform the OSC test with the standard version of GR1D described in section 2 of this paper and do not make special adjustments for the code to operate with $P = 0$. Hence, we set the pressure to a small, but non-zero value, using a polytropic EOS with $K = 10^{-20}$ and $\Gamma = 5/3$. In the artificial atmosphere outside the dust ball, we set the density to 1 g cm^{-3} . We

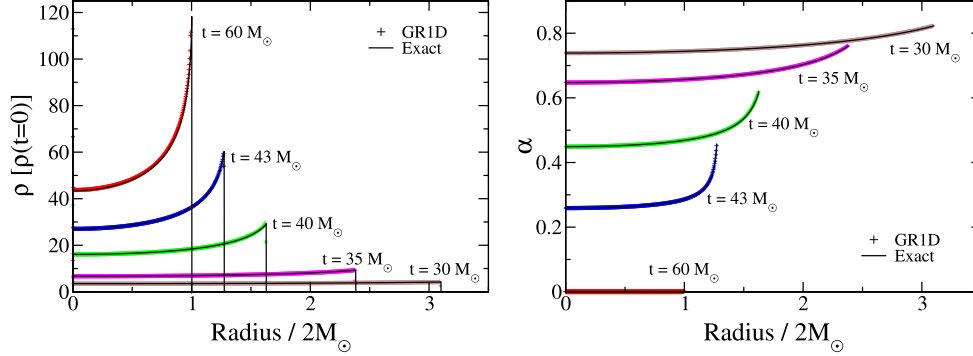


Figure 3. Oppenheimer-Snyder collapse of a pressureless dust ball. Shown are the numerical (plus symbols) and exact (solid lines) density (left panel) and lapse (right panel) profiles for various times. The density is normalized to the density at $t = 0$. The simulation uses 9000 equally spaced grid points across the domain of $20 M_{\odot}$. Initially one solar mass is distributed with constant density in a sphere of radius $10 M_{\odot}$. For clarity, we show only every third data point.

use 9000 equidistant zones to model OSC with GR1D.

In figure 3, we compare numerical and exact density and lapse profiles of OSC at $t = 30, 35, 40, 43$ and $60 M_{\odot}$. Following [34], we normalize the central density to the value at $t = 0$. The overall agreement is excellent. However, we notice two slight deviations: (1), near the origin, we observe a small build up of material. This is present also in the OSC test of [34] and probably due to diverging terms near the origin. We do not notice this effect in our stellar collapse calculations, most likely because of the stabilizing effect of the large pressure in the PNS. (2), at late times ($t > 50 M_{\odot}$), the numerical α decreases more slowly than its exact counterpart and begins to deviate significantly at $\alpha(r = 0) \lesssim 0.001$. We attribute this to numerical inaccuracies developing due (a) to the metric coefficient X becoming singular as $R_{\star} \rightarrow 2M_{\odot}$, (b) to the extreme density gradient developing at the surface at late times, and (c) to the fact that we use the standard version of GR1D without special adjustments for the OSC problem (as, e.g., made by [34]).

5.4. Hybrid Core Collapse: Convergence

In this section, we present simulations of nonrotating core collapse and present proof of convergence for GR1D. We utilize the hybrid EOS described in section 3.1, taking $\Gamma_1 = 1.28$, $\Gamma_2 = 2.5$, $\Gamma_{\text{th}} = 1.5$ and $K = 4.935 \times 10^{14} [\text{cgs}]$. Following [91], we use as initial data an $n = 3$ polytrope with a central density of $\rho_c = 5 \times 10^{10} \text{g/cm}^3$ and a K value as above and initially zero radial velocity. We simulate the evolution with GR1D for equally spaced grids of three different resolutions ($N_{\text{zones}} = 500, 1500$ and 4500) to test the self-convergence of the code. The self-convergence factor at convergence order n of a quantity q is given by,

$$Q = \frac{q_1 - q_2}{q_2 - q_3} = \frac{(dx_1)^n - (dx_2)^n}{(dx_2)^n - (dx_3)^n}, \quad (41)$$

where q_i is the numerical result from the simulation with the corresponding resolution and dx is the zone width. For this convergence test, $dx_1 = 3dx_2 = 9dx_3$. In the lower panel of figure 4, we show the self-convergence of M_{grav} at $t = -3.3$ ms (before bounce) as well as at $t = 16.6$ ms and $t = 26.6$ ms after bounce.

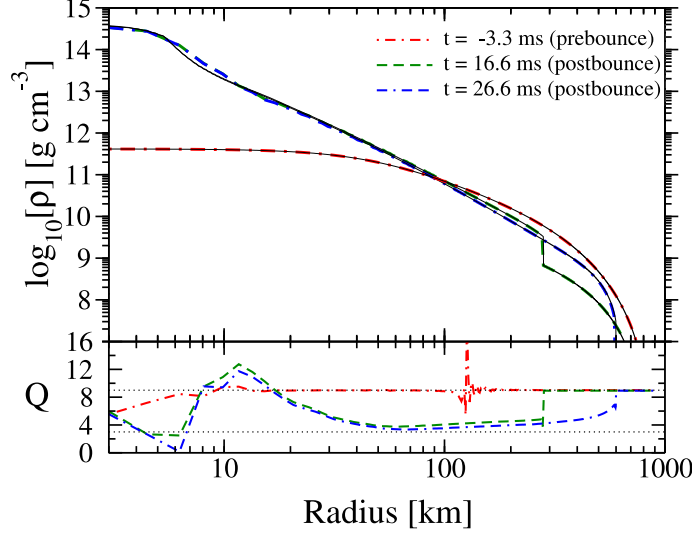


Figure 4. Radial density profiles and self-convergence for core collapse using the hybrid EOS. **Top:** Density profiles of the core collapse for various times including in the prebounce phase, and after the shock has propagated through ~ 300 and 600 km. We show the low resolution profile (segmented lines) as well as the high resolution profile (solid lines) for comparison. **Bottom:** Self-convergence of the enclosed gravitational mass, $m(r)$. Dotted lines at $Q=3$ & 9 denote expected values for 1st and 2nd order convergence.

We generally see the expected 2nd order convergence ($Q=9$) in smooth parts of the flow, but note several interesting features: (1) before bounce (red, dot-dashed curve) and near 120 km where the convergence spikes, the velocity is peaking, causing a reduction in convergence. (2), during the postbounce phase, convergence in the shocked region drops to 1st order, this is characteristic of HRSC schemes in the presence of shocks. (3), finally, during the postbounce phase for $r < 20$ km, the steepness of the density gradient at the PNS surface and the coarseness of the grid lead to *local* non-convergence. We note that the lowest resolution used here is $dx \sim 2$ km and that deviations in the density profile compared to higher-resolution simulations can be seen in the top panel of figure 4.

6. Sample Results for a $40\text{-}M_{\odot}$ Star

In the following simulations we use the single-star, non-rotating, $M_{\text{ZAMS}} = 40 M_{\odot}$, solar-metallicity presupernova model of Woosley & Weaver [88] (model s40WW95 hereafter). This model has an iron core mass of $1.98 M_{\odot}$. We set up a grid of 1000 zones that is logarithmically spaced from $r = 20$ km outward, extending to a radius of 1.15×10^5 km where the density drops to 200 g cm^{-3} . There is $14.7 M_{\odot}$ of baryonic

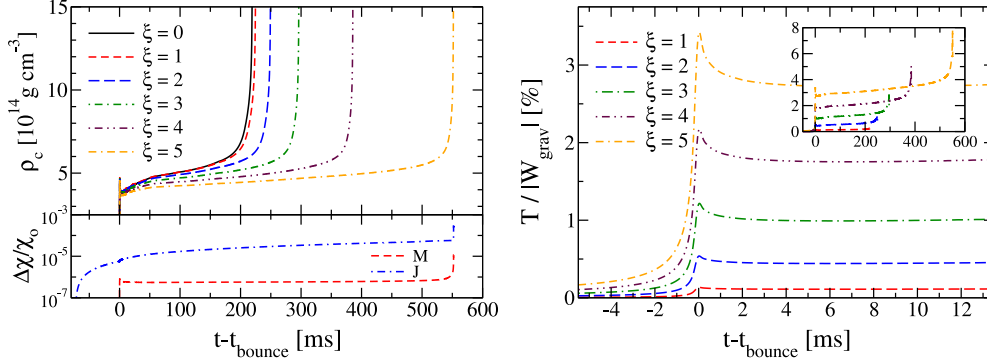


Figure 5. Black hole formation with rotation and the hybrid EOS. **Left panel:** Central densities for various initial angular velocities (top) and fractional error of the conserved quantities M_{grav} and J (bottom). **Right panel:** $T/|W_{\text{grav}}|$ near bounce and (inset) over the entire simulation. $\Omega(r)$ is set through (42).

material within this density cutoff. Inside $r = 20$ km, we use an equidistant grid with a spacing of 100 m. Such high resolution is necessary to resolve steep gradients at the PNS surface at late times ($t \gtrsim 0.5$ s). Near the origin, we increase the zone size gradually to ~ 700 m for improved stability but for rotating runs we find it necessary to maintain the fine grid spacing all the way to the origin to capture the correct angular velocity profile.

6.1. Rotating Core Collapse and Black Hole Formation in a $40\text{-}M_{\odot}$ Star using the Hybrid EOS

To show the effects of including rotation and to further demonstrate the use and usefulness of the hybrid EOS (see section 3.1) for exploratory studies, we perform a set of collapse simulations to black hole formation. We set $\Gamma_1 = 1.30$, $\Gamma_2 = 2.5$, $\Gamma_{\text{th}} = 1.34$ and impose rotation according to the rotation law (see, e.g., [77, 80])

$$\Omega(r) = \xi \frac{\pi}{10} \left[1 + \left(\frac{r}{A} \right)^2 \right]^{-1} \text{ rad s}^{-1}, \quad (42)$$

where we vary ξ from 0 to 5 and A is a parameter governing the degree of differential rotation. We choose $A = 1000$ km which leads to roughly uniform rotation within the inner core as predicted by stellar evolutionary calculations (e.g., [74]). As an additional test of GR1D, we show in the lower part of the left panel of figure 5 the relative error in total angular momentum and gravitational mass in the most rapidly spinning simulation. GR1D conserves angular momentum to better than one part in 10^4 and M_{grav} to one part in 10^6 until the onset of BH formation when the resolution becomes insufficient to fully resolve the huge gradients in the collapsing PNS.

We show in the top part of figure 5 the evolution of the central density in the simulated models. Due to the choice of Γ_1 , rotation has little influence on the prebounce dynamics [52]. The hybrid EOS qualitatively captures the stiffening of the EOS at nuclear density that leads to core bounce. Owing to the small value of

Γ_{th} , the shock stalls soon after bounce and accretion on the PNS continues. Slowly spinning models accrete rapidly and collapse to a BH after only 200 ms. Centrifugal support becomes dynamically relevant in more rapidly spinning cases, decreasing the accretion rate and delaying BH formation. The right panel of figure 5 depicts the evolution of the rotation parameter $T/|W_{\text{grav}}|$. Its systematics are very similar to what has been observed in multi-D simulations (e.g., [53, 77, 101]). $T/|W_{\text{grav}}|$ reaches a local maximum at bounce, then decreases as the PNS reaches its postbounce quasi-equilibrium. New and not shown before is the evolution of $T/|W_{\text{grav}}|$ near to BH formation. $T/|W_{\text{grav}}|$ increases only slowly after bounce (note that, in a calculation with neutrino transport or leakage, the postbounce $T/|W_{\text{grav}}|$ would increase faster [77]), but near BH formation grows nearly exponentially during PNS collapse. Rotation, in particular when it is strongly differential, can increase the maximum mass of the accreting PNS (e.g., [102]). We find[‡] BH birth masses of 1.89–1.97 M_{\odot} for the set of rotating hybrid-EOS models considered here. This increase in the maximum mass is modest, primarily because our PNS cores are rather uniformly spinning (in agreement with [53, 77]). We point out that our present treatment does not consider angular momentum redistribution by multi-dimensional effects or effective viscosity which may be present in realistic systems (see, e.g., [54, 76] and references therein).

Finally, we note that for the nonrotating ($\xi = 0$), the evolution with **GR1D** continues until a central value of the lapse function of 3×10^{-10} and a maximum value of $\sqrt{g_{rr}} = X$ of ~ 21.1 . These are excellent values in comparison to previous studies on BH formation in RGPS [30, 100]. In the rotating case, the evolution terminates somewhat earlier due primarily to numerical issues near the origin at very large v_{φ} .

6.2. Nonrotating Collapse and Black Hole Formation with Neutrino Leakage/Heating in a 40- M_{\odot} Star

In this section we show example results employing **GR1D**'s leakage/heating scheme and finite-temperature EOS. We use the s40WW95 progenitor and the LS180 EOS^{††}, $Y_e(\rho)$ parameterization pre-bounce, our standard leakage/heating scheme after bounce, and no rotation. We show results for both $f_{\text{heat}} = 0$ (losses only) and $f_{\text{heat}} = 1$. In figure 6, we compare the shock radii of these two runs and neutrino luminosities of the $f_{\text{heat}} = 1$ run (left panel) as well as the Y_e radial profiles at 50 ms after bounce (right panel). We note that the total luminosity is $L_{\nu_e} + L_{\bar{\nu}_e} + 4L_{\nu_{\mu}}$ and is corrected for redshift through (32) with $r = \infty$, but, nevertheless, is somewhat higher (up to $\sim 20\%$) than predicted by full Boltzmann radiation-hydrodynamics calculations using the same progenitor [103, 104]. The time until BH formation in the case of $f_{\text{heat}} = 1$ is $t_{\text{BH}} = 511$ ms and the baryonic mass inside the shock of the last stable configuration is 2.25 M_{\odot} . We compare this to two other studies of BH formation in 1D with the same progenitor model and EOS, but with two different implementations of GR Boltzmann neutrino transport. These studies are Fischer et al. [103] who found $t_{\text{BH}} = 435.5$ ms and 2.196 M_{\odot} and Sumiyoshi et al. [104], who found $t_{\text{BH}} = 560$ ms and 2.1 M_{\odot} . Our result is very close to these more accurate studies which gives us confidence in the

[‡] In RGPS, a coordinate singularity develops at $R = 2M$ upon BH formation. We define here the BH mass to be M_{grav} inside the radius that corresponds to the maximum X . This is an approximation and is subject to errors due to our finite resolution grid.

^{††} The lower bound on our EOS tables is 1000 g cm^{-3} , we bring the outer boundary into $\rho = 2000 \text{ g cm}^{-3}$ for this example.

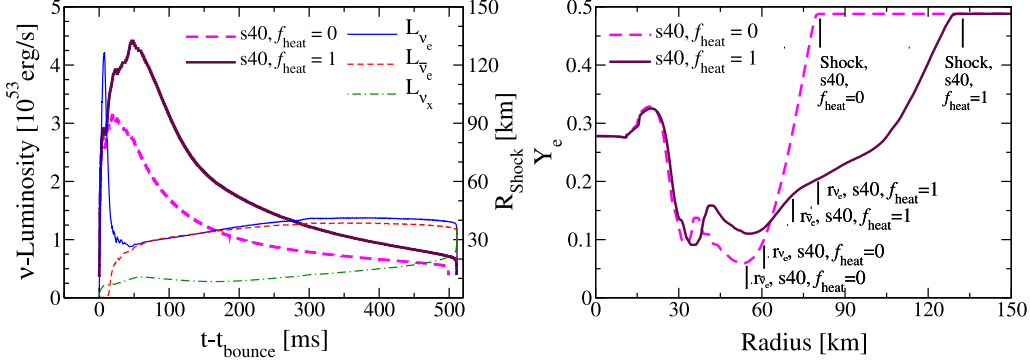


Figure 6. **Left panel:** Shock radius (thick line, right ordinate) and neutrino luminosities (thin lines, left ordinate) as a function of postbounce time in a nonrotating leakage+heating ($f_{\text{heat}} = 1$) simulation with the $40M_{\odot}$ -model of [88] run with the LS180 EOS. Shown also is the shock radius evolution (dashed thick lines) in a simulation without heating $f_{\text{heat}} = 0$. **Right panel:** Y_e profiles of both simulations at 50 ms after bounce, corresponding to the maximum shock radius of the $f_{\text{heat}} = 1$ simulation. Shock radii, electron and anti-electron neutrino neutrinospheres are marked for both the $f_{\text{heat}} = 1$ and $f_{\text{heat}} = 0$ simulations.

robustness of the heating/leakage scheme in GR1D.

The right panel of figure 6 depicts the Y_e profiles at 50 ms after bounce. The characteristic trough in Y_e behind the shock is captured by our leakage/heating scheme, but we find that our simple heating scheme converts too many of the postshock neutrons back to protons at early times, leading to too high values of Y_e in the lower postshock region between $\sim 30 - 60$ km.

To conclude this section, we note that, due to the computational efficiency of our scheme, each of our simulations took only ~ 6 CPU hours from iron core collapse through BH formation on one core of an Intel Xeon X5550 (Nehalem) machine.

7. Summary and Concluding Remarks

In this paper, we have presented the details of our new open-source Eulerian 1.5D GR hydrodynamics code GR1D. GR1D is intended primarily for the simulation of stellar collapse to neutron stars and black holes and, for the first time in the 1D GR context, includes an approximate way of accounting for stellar rotation consistent with that used in state-of-the-art calculations of stellar evolution (e.g., [74]). Using this scheme, we have presented rotating long-term postbounce simulations towards black hole formation using a $40M_{\odot}$ supernova progenitor model and showed how the simple analytic hybrid EOS can be used to capture many qualitative aspects of this phenomenon.

As we have demonstrated in this paper, GR1D performs well in standard tests and, despite its simplified neutrino leakage/heating scheme, still yields overall results in the case of failing core-collapse supernovae and black hole formation that measure up qualitatively and to some extent also quantitatively to those obtained with full

Boltzmann neutrino transport in 1D Lagrangian codes [103, 104].

Many 1D GR (radiation)-hydrodynamics formulations have been presented in the past ~ 50 years. Yet, there is presently no open-source 1D GR stellar collapse code available to the broader community. The primary motivation driving the development of **GR1D** is the need for such an open-source code that may be used as a codebase, benchmark, and testbed for improved modeling technology to be included in multi-D GR codes addressing core-collapse supernova explosions, but also failing core-collapse supernovae, black hole formation, and the post-merger evolution of binary neutron-star and neutron-star – black hole coalescence. Equipped with an approximate neutrino-leakage scheme to capture the key effects associated with neutrino heating and cooling, the version of **GR1D** discussed in this paper is a solid starting point for the next generation of astrophysically-relevant multi-D GR simulations.

The current limitations of **GR1D** due to its gray leakage and simplified heating scheme are obvious. We will continue to develop and improve **GR1D** and intend to include as a next step energy-dependent radiation transport in the multi-group flux-limited diffusion approximation (MGFLD) and/or in the isotropic diffusion source approximation (IDSA, [105]).

Acknowledgements

We thank the Niels Bohr International Academy for hosting the Microphysics in Computational Relativistics Astrophysics (MICRA) workshop in August 2009 at which much of the work presented here was inspired. It is a pleasure to thank J.-M. Ibáñez for helpful advice, for providing the original version of the code of Romero et al., and for furnishing a copy of Romero’s dissertation. We are indebted to M. Duez for very valuable help with the derivation of the neutrino source terms. We are furthermore happy to acknowledge helpful exchanges with W. D. Arnett, A. Burrows, P. Cerdá-Durán, H. Dimmelmeyer, T. Fischer, E. Gourgoulhon, I. Hawke, J. Lattimer, L. Lehner, M. Liebendörfer, E. Livne, C. Meakin, S. Noble, A. Perego, C. Pethick, E. S. Phinney, E. Schnetter, S. Scheidegger, Y. Sekiguchi, and S. Teukolsky. This work is supported by the National Science Foundation under grant numbers AST-0855535 and OCI-0905046. EOC is supported in part through a post-graduate fellowship from the Natural Sciences and Engineering Research Council of Canada (NSERC) and NASA ATP grant NNX07AH06G. We wish to thank Chris Mach for support of our group servers at TAPIR on which much of the code development and testing was carried out. Results presented in this article were obtained through computations on the NSF Teragrid under grant TG-MCA02N014, on machines of the Louisiana Optical Network Initiative under grant LONLNUMREL04, and at the National Energy Research Scientific Computing Center (NERSC), which is supported by the Office of Science of the US Department of Energy under contract DE-AC03-76SF00098.

References

- [1] H. A. Bethe. *Rev. Mod. Phys.*, **62**, 801, 1990.
- [2] M. Liebendörfer, M. Rampp, H.-T. Janka, and A. Mezzacappa. *Astrophys. J.*, **620**, 840, 2005.
- [3] R. Buras, H.-T. Janka, M. Rampp, and K. Kifonidis. *Astron. Astrophys.*, **457**, 281, 2006.
- [4] A. Marek and H.-T. Janka. *Astrophys. J.*, **694**, 664, 2009.
- [5] H.-T. Janka, K. Langanke, A. Marek, G. Martínez-Pinedo, and B. Müller. *Phys. Rep.*, **442**, 38, 2007.
- [6] A. Burrows, L. Dessart, C. D. Ott, and E. Livne. *Phys. Rep.*, **442**, 23, 2007.

- [7] S. W. Bruenn, A. Mezzacappa, W. R. Hix, J. M. Blondin, P. Marronetti, O. E. B. Messer, C. J. Dirk, and S. Yoshida. Mechanisms of Core-Collapse Supernovae and Simulation Results from the CHIMERA Code. In G. Giobbi, A. Tornambe, G. Raimondo, M. Limongi, L. A. Antonelli, N. Menci, and E. Brocato, editors, *AIP Phys. Conf. Ser.*, volume 1111 of *AIP Phys. Conf. Ser.*, page 593, 2009.
- [8] C. D. Ott. *Class. Quant. Grav.*, **26(20)**, 204015, 2009.
- [9] W. Zhang, S. E. Woosley, and A. Heger. *Astrophys. J.*, **679**, 639, 2008.
- [10] S. E. Woosley. *Astrophys. J.*, **405**, 273, 1993.
- [11] S. E. Woosley and J. S. Bloom. *Ann. Rev. Astron. Astrophys.*, **44**, 507, 2006.
- [12] M. M. May and R. H. White. *Phys. Rev.*, **141**, 1232, 1966.
- [13] C. W. Misner and D. H. Sharp. *Phys. Rev.*, **136**, 571, 1964.
- [14] J. Von Neumann and R. D. Richtmyer. *J. Appl. Phys.*, **21**, 232, 1950.
- [15] K. A. van Riper. *Astrophys. J.*, **232**, 558, 1979.
- [16] T. W. Baumgarte, S. L. Shapiro, and S. A. Teukolsky. *Astrophys. J.*, **443**, 717, 1995.
- [17] F. D. Swesty. *Astrophys. J.*, **445**, 811, 1995.
- [18] M. Liebendörfer, S. Rosswog, and F.-K. Thielemann. *Astrophys. J. Supp. Ser.*, **141**, 229, 2002.
- [19] J. A. Miralles, J. M. Ibanez, J. M. Marti, and A. Perez. *Astron. Astrophys. Suppl.*, **90**, 283–299, 1991.
- [20] P. J. Schinder, S. A. Bludman, and T. Piran. *Phys. Rev. D.*, **37**, 2722, 1988.
- [21] J. R. Wilson. *Astrophys. J.*, **163**, 209, 1971.
- [22] S. W. Bruenn. *Astrophys. J. Supp. Ser.*, **58**, 771, 1985.
- [23] E. Baron, J. Cooperstein, and S. Kahana. *Phys. Rev. Lett.*, **55**, 126, 1985.
- [24] E. Baron, E. S. Myra, J. Cooperstein, and L. J. van den Horn. *Astrophys. J.*, **339**, 978, 1989.
- [25] M. Liebendörfer, O. E. B. Messer, A. Mezzacappa, S. W. Bruenn, C. Y. Cardall, and F.-K. Thielemann. *Astrophys. J. Supp. Ser.*, **150**, 263, 2004.
- [26] J. R. Wilson. A numerical method for relativistic hydrodynamics. In L. L. Smarr, editor, *Sources of Gravitational Radiation*, page 423, 1979.
- [27] S. L. Shapiro and S. A. Teukolsky. *Astrophys. J. Lett.*, **234**, L177, 1979.
- [28] S. L. Shapiro and S. A. Teukolsky. *Astrophys. J.*, **235**, 199, 1980.
- [29] A. Mezzacappa and R. A. Matzner. *Astrophys. J.*, **343**, 853, 1989.
- [30] E.ourgoulhon. *Astron. Astrophys.*, **252**, 651, 1991.
- [31] J. M. Marti, J. M. Ibanez, and J. A. Miralles. *Astron. Astrophys.*, **235**, 535, 1990.
- [32] S. Yamada. *Astrophys. J.*, **475**, 720, 1997.
- [33] J. M. Martí, J. M. Ibáñez, and J. A. Miralles. *Phys. Rev. D.*, **43(12)**, 3794, 1991.
- [34] J. V. Romero, J. M. Ibanez, J. M. Marti, and J. A. Miralles. *Astrophys. J.*, **462**, 839, 1996.
- [35] S. C. Noble. *PhD Thesis, University of British Columbia*, *arXiv:gr-qc/0310116*, 2003.
- [36] S. Yamada, H.-T. Janka, and H. Suzuki. *Astron. Astrophys.*, **344**, 533, 1999.
- [37] K. Sumiyoshi, S. Yamada, H. Suzuki, H. Shen, S. Chiba, and H. Toki. *Astrophys. J.*, **629**, 922, 2005.
- [38] E.ourgoulhon and P. Haensel. *Astron. Astrophys.*, **271**, 187, 1993.
- [39] J. V. Romero, J. M. Miralles, J. A. Ibáñez, and J. A. Pons. General Relativistic Collapse of Hot Stellar Cores. In J. A. Miralles, J. A. Morales, & D. Saez, editor, *Some Topics on General Relativity and Gravitational Radiation*, page 289, 1997.
- [40] J. A. Pons, J. A. Miralles, and J. M. Ibáñez. General Relativistic Neutrino Transport. In J. A. Miralles, J. A. Morales, & D. Saez, editor, *Some Topics on General Relativity and Gravitational Radiation*, page 293, 1997.
- [41] T. A. Thompson, A. Burrows, and P. A. Pinto. *Astrophys. J.*, **592**, 434, 2003.
- [42] A. Burrows, E. Livne, L. Dessart, C. D. Ott, and J. Murphy. *Astrophys. J.*, **640**, 878, 2006.
- [43] A. Burrows, L. Dessart, E. Livne, C. D. Ott, and J. Murphy. *Astrophys. J.*, **664**, 416, 2007.
- [44] C. D. Ott, A. Burrows, L. Dessart, and E. Livne. *Astrophys. J.*, **685**, 1069, 2008.
- [45] F. D. Swesty and E. S. Myra. *Astrophys. J. Supp. Ser.*, **181**, 1, 2009.
- [46] A. Burrows, E. Livne, L. Dessart, C. D. Ott, and J. Murphy. *Astrophys. J.*, **655**, 416, 2007.
- [47] J. A. Isenberg. *Int. J. Mod. Phys. D*, **17**, 265, 2008.
- [48] H. Dimmelmeier, J. A. Font, and E. Müller. *Astron. Astrophys.*, **393**, 523, 2002.
- [49] H. Dimmelmeier, J. Novak, J. A. Font, J. M. Ibáñez, and E. Müller. *Phys. Rev. D.*, **71(6)**, 064023, 2005.
- [50] M. Shibata and Y. Sekiguchi. *Phys. Rev. D*, **69(8)**, 084024, 2004.
- [51] M. Shibata and Y.-I. Sekiguchi. *Phys. Rev. D.*, **71(2)**, 024014, 2005.

- [52] H. Dimmelmeier, C. D. Ott, H.-T. Janka, A. Marek, and E. Müller. *Phys. Rev. Lett.*, **98**(25), 251101, 2007.
- [53] H. Dimmelmeier, C. D. Ott, A. Marek, and H.-T. Janka. *Phys. Rev. D.*, **78**(6), 064056, 2008.
- [54] C. D. Ott, H. Dimmelmeier, A. Marek, H.-T. Janka, I. Hawke, B. Zink, and E. Schnetter. *Phys. Rev. Lett.*, **98**, 261101, 2007.
- [55] C. D. Ott, H. Dimmelmeier, A. Marek, H.-T. Janka, B. Zink, I. Hawke, and E. Schnetter. *Class. Quant. Grav.*, **24**, 139, 2007.
- [56] B. Müller. *Multi-dimensional relativistic simulations of core-collapse supernovae with energy-dependent neutrino transport*. PhD thesis, Technische Universität München, München, Germany, 2009.
- [57] R. Buras, M. Rampp, H.-T. Janka, and K. Kifonidis. *Astron. Astrophys.*, **447**, 1049, 2006.
- [58] B. Müller, H.-T. Janka, and H. Dimmelmeier. *Submitted to Astrophys. J. Supp. Ser.*, *arXiv:1001.4841 [astro-ph]*, 2010.
- [59] URL <http://www.whiskycode.org/>. Whisky, EU Network GR Hydrodynamics Code.
- [60] J. M. Lattimer and F. D. Swesty. *Nucl. Phys. A*, **535**, 331, 1991.
- [61] H. Shen, H. Toki, K. Oyamatsu, and K. Sumiyoshi. *Nucl. Phys. A*, **637**, 435, 1998. URL [http://user.numazu-ct.ac.jp/~sim\\$sumi/eos](http://user.numazu-ct.ac.jp/~sim$sumi/eos).
- [62] H. Shen, H. Toki, K. Oyamatsu, and K. Sumiyoshi. *Prog. Th. Phys.*, **100**, 1013, 1998.
- [63] M. Liebendörfer. *Astrophys. J.*, **633**, 1042, 2005.
- [64] M. Ruffert, H.-T. Janka, and G. Schaefer. *Astron. Astrophys.*, **311**, 532, 1996.
- [65] S. Rosswog and M. Liebendörfer. *Mon. Not. Roy. Astron. Soc.*, **342**, 673, 2003.
- [66] F. Banyuls, J. A. Font, J. M. Ibáñez, J. M. Martí, and J. A. Miralles. *Astrophys. J.*, **476**, 221, 1997.
- [67] J. A. Font, M. Miller, W.-M. Suen, and M. Tobias. *Phys. Rev. D.*, **61**(4), 044011–+, 2000.
- [68] J. A. Font. *Liv. Rev. Rel.*, **11**, 7, 2008.
- [69] James M. Hyman. The method of lines solution of partial differential equations. Technical Report COO-3077-139, ERDA Mathematics and Computing Laboratory, Courant Institute of Mathematical Sciences, New York University, 1976.
- [70] P. Colella and P. R. Woodward. *J. Comp. Phys.*, **54**, 174–201, 1984.
- [71] B. J. van Leer. *J. Comp. Phys.*, **23**, 276, 1977.
- [72] B. Einfeldt. On Godunov type methods for the Euler equations with a general equation of state. In *Shock tubes and waves; Proceedings of the Sixteenth International Symposium, Aachen, Germany, July 26-31, 1987 (A89-12876 03-34)*. Weinheim, Germany, VCH Verlagsgesellschaft mbH, 1988, p. 671-676., pages 671–676, 1988.
- [73] A. S. Endal and S. Sofia. *Astrophys. J.*, **220**, 279, 1978.
- [74] A. Heger, N. Langer, and S. E. Woosley. *Astrophys. J.*, **528**, 368, 2000.
- [75] R. Hirschi, G. Meynet, and A. Maeder. **425**, 649–670, 2004.
- [76] T. A. Thompson, E. Quataert, and A. Burrows. *Astrophys. J.*, **620**, 861, 2005.
- [77] C. D. Ott, A. Burrows, T. A. Thompson, E. Livne, and R. Walder. *Astrophys. J. Suppl. Ser.*, **164**, 130, 2006.
- [78] G. B. Cook, S. L. Shapiro, and S. A. Teukolsky. *Astrophys. J.*, **398**, 203–223, 1992.
- [79] H.-T. Janka, T. Zwerger, and R. Mönchmeyer. *Astron. Astrophys.*, **268**, 360, 1993.
- [80] T. Zwerger and E. Müller. *Astron. Astrophys.*, **320**, 209, 1997.
- [81] J. S. Read, B. D. Lackey, B. J. Owen, and J. L. Friedman. *Phys. Rev. D.*, **79**(12), 124032, 2009.
- [82] L. S. Shapiro and S. A. Teukolsky. *Black Holes, White Dwarfs and Neutron Stars*. John Wiley & Sons, New York U. S. A., 1983.
- [83] J. M. Lattimer, C. J. Pethick, D. G. Ravenhall, and D. Q. Lamb. *Nuc. Phys. A*, **432**, 646, 1985.
- [84] F. X. Timmes and D. Arnett. *Astrophys. J. Supp. Ser.*, **125**, 277, 1999.
- [85] M. Rampp and H.-T. Janka. *Astron. Astrophys.*, **396**, 361, 2002.
- [86] F. X. Timmes and F. D. Swesty. *Astrophys. J. Supp. Ser.*, **126**, 501, 2000.
- [87] M. Steffen. *Astron. Astrophys.*, **239**, 443, 1990.
- [88] S. E. Woosley and T. A. Weaver. *Astrophys. J. Supp. Ser.*, **101**, 181, 1995.
- [89] H.-T. Janka. *Astron. Astrophys.*, **368**, 527, 2001.
- [90] K. Takahashi, M. F. El Eid, and W. Hillebrandt. *Astron. Astrophys.*, **67**, 185, 1978.
- [91] C. D. Ott. *Stellar Iron Core Collapse in 3+1 General Relativity and The Gravitational Wave Signature of Core-Collapse Supernovae*. PhD thesis, Universität Potsdam, Potsdam, Germany, 2006. URL <http://nbn-resolving.de/urn/resolver.pl?urn=urn:nbn:de:kobv:517-opus-12986>.
- [92] S. A. Bludman and K. A. van Riper. *Astrophys. J.*, **212**, 859–872, 1977.
- [93] J. M. Martí and E. Müller. *Liv. Rev. Rel.*, **6**, 7, 2003.

- [94] H. Dimmelmeier, J. A. Font, and E. Müller. *Astron. Astrophys.* , **388**, 917, 2002.
- [95] L. I. Sedov. *Similarity and Dimensional Methods in Mechanics*. 1959.
- [96] E. J. Tasker, R. Brunino, N. L. Mitchell, D. Michielsen, S. Hopton, F. R. Pearce, G. L. Bryan, and T. Theuns. *Mon. Not. Roy. Astron. Soc.* , **390**, 1267–1281, 2008.
- [97] P. Anninos, P. C. Fragile, and J. D. Salmonson. *Astrophys. J.*, **635**, 723, 2005.
- [98] J. R. Oppenheimer and G. M. Volkoff. *Phys. Rev.*, **55**, 374, 1939.
- [99] L. I. Petrich, S. L. Shapiro, and S. A. Teukolsky. *Phys. Rev. D.*, **33**, 2100–2110, 1986.
- [100] E.ourgoulhon. *Ann. Phys.*, **18**, 1, 1993.
- [101] C. D. Ott, A. Burrows, E. Livne, and R. Walder. *Astrophys. J.*, **600**, 834, 2004.
- [102] T. W. Baumgarte, S. L. Shapiro, and M. Shibata. *Astrophys. J. Lett.*, **528**, L29, 2000.
- [103] T. Fischer, S. C. Whitehouse, A. Mezzacappa, F.-K. Thielemann, and M. Liebendörfer. *Astron. Astrophys.* , **499**, 1–15, 2009.
- [104] K. Sumiyoshi, S. Yamada, and H. Suzuki. *Astrophys. J.*, **667**, 382, 2007.
- [105] M. Liebendörfer, T. Fischer, C. Fröhlich, F.-K. Thielemann, and S. Whitehouse. *J. Phys. G Nuc. Phys.*, **35**(1), 014056, 2008.
- [106] C. W. Misner, K. S. Thorne, and J. A. Wheeler. *Gravitation*. San Francisco: W.H. Freeman and Co., 1973.

Appendix A. Evolution Equation Derivation

In this appendix we derive the evolution equations for the conserved variables D, DY_e, S^r, S_ϕ and τ used in **GR1D** and presented in section 2.2 and 2.3. **GR1D** uses the spherically symmetric metric $g_{\mu\nu} = \text{diag}(-\alpha^2, X^2, r^2, r^2 \sin^2 \theta)$ with $\alpha = \exp(\Phi(r, t))$ with $\Phi(r, t)$ defined through (5), $X = (1 - \frac{2m(r, t)}{r})^{-1/2}$ where $m(r, t)$ is the enclosed gravitational mass at coordinate radius r . We assume the matter to be a perfect fluid described by a mass current density of $J^\mu = \rho u^\mu$ and a stress-energy tensor, $T^{\mu\nu} = \rho h u^\mu u^\nu + g^{\mu\nu} P$ where ρ is the rest mass density, P is the fluid pressure, $h = 1 + \epsilon + P/\rho$ is the specific enthalpy with ϵ the specific internal energy; $u^\mu = (W/\alpha, Wv/X, 0, 0)$ is the fluid 4-velocity (without taking into account rotation) with $W = 1/\sqrt{1 - v^2}$ is the Lorentz factor and v is the physical radial velocity.

While evaluating the covariant derivative of the stress-energy tensor and matter current density, we make use of the following formula,

$$\nabla_\mu J^\mu = \frac{1}{\sqrt{-g}} (\sqrt{-g} J^\mu)_{,\mu} \quad (\text{A.1})$$

and

$$\nabla_\mu T^{\mu\nu} = \frac{1}{\sqrt{-g}} (\sqrt{-g} T^{\mu\nu})_{,\mu} + \Gamma^\nu_{\alpha\mu} T^{\mu\alpha}, \quad (\text{A.2})$$

where $\sqrt{-g} = \alpha X r^2$ is the determinant of the metric and $\Gamma^\nu_{\alpha\mu}$ are Christoffel symbols and are defined through derivatives of the metric,

$$\Gamma^\nu_{\alpha\mu} = \frac{1}{2} g^{\nu\beta} (g_{\mu\beta, \alpha} + g_{\alpha\beta, \mu} - g_{\alpha\mu, \beta}). \quad (\text{A.3})$$

For our metric, all non-zero Christoffels are given in Table A1, $\Gamma^\nu_{\alpha\mu}$ is symmetric in the last two indices, duplicates are omitted.

It is useful to note the following derivatives needed in the derivation of the evolution equations:

$$\partial_r \Phi(r, t) = X^2 \left[\frac{m}{r^2} + 4\pi r (P + \rho h W^2 v^2) \right], \quad (\text{A.4})$$

$\Gamma_{tt}^t = \partial_t \phi(r, t)$	$\Gamma_{\theta\theta}^r = -\frac{r}{X^2}$
$\Gamma_{tr}^t = \partial_r \phi(r, t)$	$\Gamma_{\phi\phi}^r = -\frac{r \sin^2 \theta}{X^2}$
$\Gamma_{rr}^t = \alpha^{-2} \frac{X^4}{r} \partial_t m(r, t)$	$\Gamma_{r\theta}^\theta = \frac{1}{r}$
$\Gamma_{tt}^r = \frac{\alpha^2}{X^2} \partial_r \phi(r, t)$	$\Gamma_{\phi\phi}^\theta = -\sin \theta \cos \theta$
$\Gamma_{tr}^r = \frac{X^2}{r} \partial_t m(r, t)$	$\Gamma_{r\phi}^\phi = \frac{1}{r}$
$\Gamma_{rr}^r = \frac{X^2}{r} (\partial_r m(r, t) - \frac{m(r, t)}{r})$	$\Gamma_{\theta\phi}^\phi = \frac{\cos \theta}{\sin \theta}$

Table A1. Connection coefficients.

$$\partial_r X = X^3 \left[\frac{\partial_r m}{r} - \frac{m}{r^2} \right], \quad (\text{A.5})$$

$$\partial_t X = X^3 \frac{\partial_t m}{r}, \quad (\text{A.6})$$

$$\partial_r m = 4\pi r^2 (\rho h W^2 - P), \quad (\text{A.7})$$

$$\partial_t m = -4\pi r^2 \frac{\alpha \rho h W^2 v}{X}. \quad (\text{A.8})$$

Appendix A.1. Source Terms

The evolution equations follow from $\nabla_\mu J^\mu = 0$ and $\nabla_\mu T^{\mu\nu} = 0$. Since we treat neutrinos through a leakage scheme, we add in neutrino source terms explicitly to the RHS of these equations. The neutrino physics of **GR1D** occurs in the rest frame of the fluid; in this frame the energy and lepton rates are calculated with the neutrino leakage scheme, Q_E^0 and $R_{Y_e}^0$ are given in (34). Momentum exchange in the fluid rest frame is taken into account approximately via $Q_M^0 = -\frac{\partial P_\nu}{\partial r}$ where the gradient is evaluated numerically in the coordinate frame. This introduces a slight inconsistency, since in a full radiation-transport treatment the momentum transfer is computed fully locally via the second angular moment of the local neutrino radiation intensity [58].

By writing the evolution equations in the comoving orthonormal frame of the fluid (fluid rest frame, [FRF]) with 4-velocity $\vec{u} = (1, 0, 0, 0)_{\text{FRF}}$ and unit radial normal $\vec{n} = (0, 1, 0, 0)_{\text{FRF}}$ and expressing them as frame-independent tensor equations we can derive expressions for the evolution equations in any frame. For the lepton fraction,

$$\begin{aligned} \partial_t(\rho Y_e) &= R_{Y_e}^0, \\ \partial_t(\rho Y_e u^t) &= R_{Y_e}^0, \\ \partial_\mu(\rho Y_e u^\mu) &= R_{Y_e}^0, \\ \nabla_\mu(\rho Y_e u^\mu) &= R_{Y_e}^0. \end{aligned} \quad (\text{A.9})$$

We write the energy and momentum source terms in the fluid rest frame as a 4-vector, $\vec{q} = (Q_E^0, Q_M^0, 0, 0)_{\text{FRF}}$ or in frame-independent notation, $Q_E^0 \vec{u} + Q_M^0 \vec{n}$. In the fluid rest frame, the evolution equations for energy and momentum become,

$$\partial_t T^{tt} = Q_E^0 = q^t, \quad (\text{A.10})$$

and

$$\partial_t T^{tr} = Q_M^0 = q^r, \quad (\text{A.11})$$

or in frame-independent tensor notation,

$$\nabla_\mu T^{\mu\nu} = q^\nu. \quad (\text{A.12})$$

For the evolution equations, we must transform \vec{q} from the fluid rest frame, to the coordinate frame (CF) of **GR1D**. In a general frame \vec{n} is a vector that is both *i*) normalized and *ii*) orthogonal to \vec{u} . In the CF of **GR1D**, where \vec{u} is the 4-velocity, these two conditions (along with the assumption of spherical symmetry) on \vec{n} give $\vec{n} = (Wv/\alpha, W/X, 0, 0)_{\text{CF}}$. \vec{q} in the CF then becomes $\vec{q} = (\frac{W}{\alpha}(Q_E^0 + vQ_M^0), \frac{W}{X}(vQ_E^0 + Q_M^0), 0, 0)_{\text{CF}}$. This can also be derived via a Lorentz transformation. In principle, non-zero rotation will give rise to source terms for the ϕ -momentum evolution through q^ϕ and modify the radial source terms q^r . In consideration of the significant approximations already present in both our neutrino leakage scheme and in our treatment of rotation, we neglect the influence of rotation on the source terms. This is justified as long as $v_\phi \ll c$.

Appendix A.2. GR1D Evolution Equations

In the coordinate frame of **GR1D** where $u^\mu = (W/\alpha, Wv/X, 0, 0)$, the continuity equation, $\nabla_\mu J^\mu = 0$ gives the evolution of the rest mass density,

$$\begin{aligned} \nabla_\mu(\rho u^\mu) &= 0, \\ \frac{1}{\sqrt{-g}} \left[\partial_t \left(\sqrt{-g} \frac{\rho W}{\alpha} \right) + \partial_r \left(\sqrt{-g} \frac{\rho W v}{X} \right) \right] &= 0, \\ \partial_t(D) + \frac{1}{r^2} \partial_r \left(\frac{\alpha r^2}{X} D v \right) &= 0. \end{aligned} \quad (\text{A.13})$$

The evolution of the electron fraction Y_e follows a similar derivation but contains a source term from the neutrino leakage scheme. In the coordinate frame of **GR1D** (A.9) becomes,

$$\begin{aligned} \nabla_\mu(\rho Y_e u^\mu) &= R_{Y_e}^0, \\ \frac{1}{\sqrt{-g}} \left[\partial_t \left(\sqrt{-g} \frac{\rho W Y_e}{\alpha} \right) + \partial_r \left(\sqrt{-g} \frac{\rho W Y_e v}{X} \right) \right] &= R_{Y_e}^0, \\ \frac{1}{\alpha X} \left[\partial_t (X \rho W Y_e) + \frac{1}{r^2} \partial_r \left(\frac{\alpha r^2}{X} X \rho W Y_e v \right) \right] &= R_{Y_e}^0, \\ \partial_t(D Y_e) + \frac{1}{r^2} \partial_r \left(\frac{\alpha r^2}{X} D Y_e v \right) &= \alpha X R_{Y_e}^0. \end{aligned} \quad (\text{A.14})$$

The momentum evolution equation for **GR1D** is obtained by evaluating (A.12) with $\nu = r$.

$$\begin{aligned} \nabla_\mu T^{\mu r} &= q^r, \\ (\sqrt{-g} T^{\mu r})_{,\mu} &= \sqrt{-g} q^r - \sqrt{-g} \Gamma_{\nu\mu}^r T^{\mu\nu}, \\ \partial_t(\rho h W^2 v) + \frac{1}{r^2} \partial_r \left(\frac{\alpha r^2}{X} (\rho h W^2 v^2 + P) \right) &= \alpha X q^r - \alpha X (\Gamma_{\nu t}^r T^{t\nu} + \Gamma_{\nu r}^r T^{r\nu} \\ &\quad + \Gamma_{\nu\phi}^r T^{\phi\nu} + \Gamma_{\nu\theta}^r T^{\theta\nu}), \\ \partial_t(S^r) + \frac{1}{r^2} \partial_r \left(\frac{\alpha r^2}{X} (S^r v + P) \right) &= \alpha X q^r - \alpha X (\Gamma_{tt}^r T^{tt} + \Gamma_{rt}^r T^{tr} \end{aligned}$$

$$\begin{aligned}
& + \Gamma_{tr}^r T^{rt} + \Gamma_{rr}^r T^{rr} + \Gamma_{\phi\phi}^r T^{\phi\phi} + \Gamma_{\theta\theta}^r T^{\theta\theta} \Big), \\
\partial_t(S^r) + \frac{1}{r^2} \partial_r \left(\frac{\alpha r^2}{X} (S^r v + P) \right) & = -\alpha X \left[2 \frac{X}{r} \frac{\rho h W^2 v}{\alpha X} \partial_t m \right. \\
& + \frac{X^2}{r} \left(\partial_r m - \frac{m}{r} \right) \left(\frac{\rho h W^2 v^2 + P}{X^2} \right) \\
& - \frac{2P}{X^2 r} + \frac{\alpha^2}{X^2} \frac{\rho h W^2 - P}{\alpha^2} \partial_r \Phi \Big] + \alpha X q^r, \\
\partial_t(S^r) + \frac{1}{r^2} \partial_r \left[\frac{\alpha r^2}{X} (S^r v + P) \right] & = \alpha X \left[(S^r v - \tau - D) \left(8\pi r P + \frac{m}{r^2} \right) \right. \\
& + \frac{Pm}{r^2} + \frac{2P}{X^2 r} \Big] + \alpha W (v Q_E^0 + Q_M^0). \quad (\text{A.15})
\end{aligned}$$

where in the last step we have reorganized the source terms to the form of [34] using the derivatives defined in (A.4)-(A.8). If non-zero, $u^\phi = W v_\phi / r$ leads to an additional term $(\alpha \rho h W^2 v_\phi^2 \sin(\theta)^2 / X r)$ arising through $\Gamma_{\phi\phi}^r T^{\phi\phi}$ on the RHS of A.15, averaging this term over the spherical shell gives $2/3 \alpha \rho h W^2 v_\phi^2 / X r$. When rotation is included, the evolution equation for $S_\phi = \rho h W^2 v_\phi r$ is,

$$\begin{aligned}
\nabla_\mu T_\phi^\mu & = 0, \\
\left(\sqrt{-g} T_\phi^\mu \right)_{,\mu} & = \sqrt{-g} \Gamma_{\phi\mu}^\nu T_\nu^\mu, \\
\partial_t (\alpha X r^2 g_{\phi\phi} T^{t\phi}) + \partial_r (\alpha X r^2 g_{\phi\phi} T^{r\phi}) & = \sqrt{-g} \left(\Gamma_{\phi\phi}^r T_r^\phi + \Gamma_{\phi r}^\phi T_\phi^r \right), \\
\partial_t (X \rho h W^2 v_\phi r) + \frac{1}{r^2} \partial_r \left(\frac{\alpha r^2}{X} \rho h W^2 v_\phi r v X \right) & = 0, \\
\partial_t (S_\phi) + \frac{1}{r^2} \partial_r \left(\frac{\alpha r^2}{X} S_\phi v \right) & = \frac{\rho h W^2 v_\phi r}{X} \left(-\partial_t X - \frac{\alpha v}{X} \partial_r X \right), \\
\partial_t (S_\phi) + \frac{1}{r^2} \partial_r \left(\frac{\alpha r^2}{X} S_\phi v \right) & = \alpha \rho h W^2 v_\phi v X \left(4\pi r^2 P + \frac{m}{r} \right). \quad (\text{A.16})
\end{aligned}$$

The energy evolution equation for GR1D is derived by taking $\nu = t$ in (A.12),

$$\begin{aligned}
\nabla_\mu T^{\mu t} & = q^t, \\
\left(\sqrt{-g} T^{\mu t} \right)_{,\mu} & = \sqrt{-g} q^t - \sqrt{-g} \Gamma_{\nu\mu}^t T^{\mu\nu}, \\
\partial_t \left(\frac{X}{\alpha} (\rho h W^2 - P) \right) + \frac{1}{r^2} \partial_r \left(\frac{\alpha r^2}{X} \rho h W^2 v \frac{X}{\alpha} \right) & = \alpha X q^t - \alpha X (\Gamma_{t\mu}^t T^{\mu t} + \Gamma_{r\mu}^t T^{\mu r}), \\
\frac{X}{\alpha} \left[\partial_t (\tau + D) + \frac{1}{r^2} \partial_r \left(\frac{\alpha r^2}{X} S^r \right) \right] & = \alpha X q^t - \alpha X (\Gamma_{tt}^t T^{tt} + 2\Gamma_{tr}^t T^{rt} \\
& + \Gamma_{rr}^t T^{rr}) - (\rho h W^2 - P) \partial_t \left(\frac{X}{\alpha} \right) \\
& - \frac{\alpha \rho h W^2 v}{X} \partial_r \left(\frac{X}{\alpha} \right),
\end{aligned}$$

$$\begin{aligned}
\partial_t(\tau + D) + \frac{1}{r^2} \partial_r \left(\frac{\alpha r^2}{X} S^r \right) &= \alpha^2 q^t, \\
\partial_t(\tau) + \frac{1}{r^2} \partial_r \left(\frac{\alpha r^2}{X} (S^r - Dv) \right) &= \alpha W (Q_E^0 + v Q_M^0). \tag{A.17}
\end{aligned}$$

where in the last step we use the continuity equation (A.13) to subtract out the evolution of the rest mass density, obtaining the evolution equation for τ . A non-zero u^ϕ does not contribute source terms to this evolution equation.

Appendix B. Neutrino Luminosities

The luminosity computed from the neutrino leakage scheme is derived in the rest frame of the fluid. We require knowledge of the neutrino luminosity as measured by an observer at rest in the coordinate frame to determine *i*) the luminosity measured by an observer at rest at infinity and *ii*) the luminosity in the fluid rest frame at some other coordinate radius for our neutrino heating scheme. We derive these relationships by assuming the neutrinos are emitted radially in the fluid rest frame with energy E^{FRF} .

In the fluid rest frame (FRF), the 4-momentum of the (massless) neutrino is $p^a = (E^{\text{FRF}}, E^{\text{FRF}}, 0, 0)_{\text{FRF}}$. We use the orthonormal tetrad in Appendix A.1, in the fluid frame, $\vec{u} = \vec{e}_0 = (1, 0, 0, 0)_{\text{FRF}}$ and $\vec{n} = \vec{e}_1 = (0, 1, 0, 0)_{\text{FRF}}$, in the coordinate frame (CF), $u^\beta = e_0^\beta = (W/\alpha, Wv/X, 0, 0)_{\text{CF}}$ and $n^\beta = e_1^\beta = (Wv/\alpha, W/X, 0, 0)_{\text{CF}}$. In this we have neglected rotational effects which will be small for $v_\varphi \ll c$. Transforming p^a to the coordinate basis of GR1D,

$$p^\beta = p^a e_a^\beta = E^{\text{FRF}} \left(\frac{W}{\alpha} (1+v), \frac{W}{X} (1+v), 0, 0 \right)_{\text{CF}}. \tag{B.1}$$

An observer at rest in the coordinate frame ($U^\alpha = (1, 0, 0, 0)_{\text{CF}}$) then sees the neutrino with energy,

$$E^{\text{CF}} = -\vec{p} \cdot \vec{U} = -g_{\alpha\beta} p^\beta U^\alpha = \alpha^2 E^{\text{FRF}} \frac{W}{\alpha} (1+v) = \alpha W (1+v) E^{\text{FRF}}. \tag{B.2}$$

Noting that (see [106], eq. 25.25), for massless particles emitted from rest at r and observed by an observer at rest at r' , $\lambda(r)|g_{00}(r)|^{-1/2} = \lambda(r')|g_{00}(r')|^{-1/2}$ implies,

$$\frac{E^{\text{CF}}(r')}{E^{\text{CF}}(r)} = \frac{\lambda_r}{\lambda_{r'}} = \frac{|g_{00}(r)|^{1/2}}{|g_{00}(r')|^{1/2}} = \frac{\alpha(r)}{\alpha(r')}, \tag{B.3}$$

this is the redshift formula for particles leaving a gravitational well.